

**Numerical Investigation of Hexacopter Downwash Airflow  
Field at Various Flight Speeds and Heights for Agricultural  
Spraying Operation.**



By

Muhammad Yawar Abbas

(Registration No: 00000329977)

Department of Mechanical Engineering

School of Mechanical and Manufacturing Engineering

National University of Sciences & Technology (NUST)

Islamabad, Pakistan

(2024)

**Numerical Investigation of Hexacopter Downwash Airflow  
Field at Various Flight Speeds and Heights for Agricultural  
Spraying Operation.**



By

Muhammad Yawar Abbas

(Registration No: 00000329977)

A thesis submitted to the National University of Sciences and Technology, Islamabad,

in partial fulfillment of the requirements for the degree of

Master of Science in  
Mechanical Engineering

Supervisor: Dr. Zaib Ali

School of Mechanical and Manufacturing Engineering

National University of Sciences & Technology (NUST)

Islamabad, Pakistan

(2024)

## THESIS ACCEPTANCE CERTIFICATE

Certified that final copy of MS/MPhil thesis written by **Regn No. 00000329977 Muhammad yawar Abbas** of **School of Mechanical & Manufacturing Engineering (SMME)** has been vetted by undersigned, found complete in all respects as per NUST Statues/Regulations, is free of plagiarism, errors, and mistakes and is accepted as partial fulfillment for award of MS/MPhil degree. It is further certified that necessary amendments as pointed out by GEC members of the scholar have also been incorporated in the said thesis titled. **Numerical Investigation of Hexacopter Downwash Airflow field at Various Flight Speeds and Heights for Agricultural Spraying Operation.**


Signature:



Name (Supervisor): Zaib Ali

Date: 27 - Aug - 2024

Signature (HOD):



Date: 27 - Aug - 2024

Signature (DEAN):




Date: 27 - Aug - 2024




National University of Sciences & Technology (NUST)  
**MASTER'S THESIS WORK**

We hereby recommend that the dissertation prepared under our supervision by: Muhammad yawar Abbas (00000329977)  
Titled: Numerical Investigation of Hexacopter Downwash Airflow field at Various Flight Speeds and Heights for Agricultural Spraying Operation. be accepted in partial fulfillment of the requirements for the award of MS in Mechanical Engineering degree.

**Examination Committee Members**

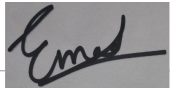
1. Name: Emad Ud Din Signature: 

2. Name: Waqas Khalid Signature: 

Supervisor: Zaib Ali

Signature: 

Date: 27 - Aug - 2024



Head of Department

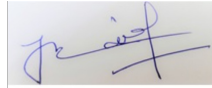
27 - Aug - 2024

Date

**COUNTERSIGNED**

27 - Aug - 2024

Date



Dean/Principal

.....

## CERTIFICATE OF APPROVAL

This is to certify that the research work presented in this thesis, entitled “Numerical Investigation of Hexacopter Downwash Airflow Field at Various Flight Speeds and Heights for Agricultural Spraying Operation.” was conducted by Mr. Muhammad Yawar Abbas under the supervision of Dr. Zaib Ali.

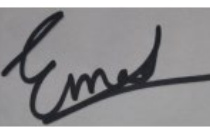
No part of this thesis has been submitted anywhere else for any other degree. This thesis is submitted to the Department of Mechanical Engineering, SMME, NUST in partial fulfillment of the requirements for the degree of Master of Science in Field of Mechanical Engineering Department of Mechanical Engineering, SMME, National University of Sciences and Technology, Islamabad.

Student Name: Muhammad Yawar Abbas

Signature: 

Examination Committee:

a) External Examiner 1: Dr. Emad Ud Din  
(Professor & SMME,NUST)

Signature: 

.....

b) External Examiner 2: Dr. Waqas Khalid  
(Assistant Professor & SMME, NUST)


Signature: 

.....

Supervisor Name: Dr. Zaib Ali

Signature: 

Name of Dean/HOD: Dr. Mian Ashfaq Ali

Signature: 

## **AUTHOR'S DECLARATION**

I Muhammad Yawar Abbas hereby state that my MS thesis titled “Numerical Investigation of Hexacopter Downwash Airflow field at Various Flight Speeds and Heights for Agricultural Spraying Operation.” is my own work and has not been submitted previously by me for taking any degree from National University of Sciences and Technology, Islamabad or anywhere else in the country/ world.

At any time if my statement is found to be incorrect even after I graduate, the university has the right to withdraw my MS degree.

Name of Student: Muhammad Yawar Abbas


Date: August 20, 2024

## **PLAGIARISM UNDERTAKING**

I solemnly declare that research work presented in the thesis titled “Numerical Investigation of Hexacopter Downwash Airflow field at Various Flight Speeds and Heights for Agricultural Spraying Operation.” is solely my research work with no significant contribution from any other person. Small contribution/ help wherever taken has been duly acknowledged and that complete thesis has been written by me.

I understand the zero-tolerance policy of the HEC and National University of Sciences and Technology (NUST), Islamabad towards plagiarism. Therefore, I as an author of the above titled thesis declare that no portion of my thesis has been plagiarized and any material used as reference is properly referred/cited.

I undertake that if I am found guilty of any formal plagiarism in the above titled thesis even after award of MS degree, the University reserves the rights to withdraw/revoke my MS degree and that HEC and NUST, Islamabad has the right to publish my name on the HEC/University website on which names of students are placed who submitted plagiarized thesis.

Student Signature:  \_\_\_\_\_

Name: Muhammad Yawar Abbas

# TABLE OF CONTENTS

<b>TABLE OF CONTENTS</b>	<b>VIII</b>
<b>LIST OF TABLES</b>	<b>X</b>
<b>LIST OF FIGURES</b>	<b>XI</b>
<b>LIST OF SYMBOLS, ABBREVIATIONS AND ACRONYMS</b>	<b>XII</b>
<b>ABSTRACT</b>	<b>XIII</b>
<b>CHAPTER 1: INTRODUCTION</b>	<b>1</b>
<b>1.1 Background</b>	<b>1</b>
<b>1.2 Problem Statement</b>	<b>2</b>
<b>1.3 Research Aims</b>	<b>2</b>
<b>1.4 Significance of Study</b>	<b>2</b>
<b>CHAPTER 2: LITERATURE REVIEW.</b>	<b>3</b>
<b>2.1 Agricultural UAVs in Farming</b>	<b>3</b>
<b>2.2 Simulation Tools</b>	<b>3</b>
<b>2.3 Lattice Boltzmann Method in Fluid Dynamics</b>	<b>5</b>
<b>2.4 XFlow as a CFD Approach</b>	<b>7</b>
<b>2.5 Previous Studies</b>	<b>7</b>
<b>CHAPTER 3: METHODOLOGY</b>	<b>10</b>
<b>3.1 Lattice Boltzmann Method</b>	<b>10</b>
3.1.1 Lattice Scheme	10
3.1.2 Propagate-Collide Scheme	13
3.1.3 Boundary Conditions	18
<b>3.2 XFlow as an Advanced CFD Approach</b>	<b>20</b>
3.2.1 Octree Lattice Structure	21
3.2.2 Lattice Boltzmann Method using Central-Moment	22
3.2.3 Turbulence Modeling	23
<b>3.3 Scanning of Propeller Blade</b>	<b>25</b>
<b>3.4 Development of Hexa-copter Geometry</b>	<b>25</b>
<b>3.5 Downwash Analysis utilizing XFlow</b>	<b>26</b>
3.5.1 Environment	27
3.5.2 Geometry	29
3.5.3 Pre-Processing	30
<b>CHAPTER 4: RESULTS AND DISCUSSIONS</b>	<b>34</b>
<b>4.1 Downwash Airflow field</b>	<b>34</b>
<b>4.2 Evaluating Index</b>	<b>36</b>
<b>4.3 Downwash Airflow field at Various Flight Speeds and Heights</b>	<b>36</b>



4.3.1 Volumetric Velocity Field	37
4.3.2 Distribution of V-y on the PDAF	39
4.3.3 The penetrable and coverage area	41
<b>CHAPTER:5 CONCLUSION</b>	<b>45</b>
<b>CHAPTER 6: FUTURE WORK AND RECOMMENDATIONS</b>	<b>47</b>
<b>REFERENCES</b>	<b>48</b>

## LIST OF TABLES

	<b>Page No.</b>
Table 1 - Lattice resolutions and adaptive wake refinement threshold values .....	31
Table 2 Parameters for study of airflow field .....	37

# LIST OF FIGURES

	<b>Page No.</b>
Figure 3.1 Velocities discretization on a D2Q9 lattice scheme .....	11
Figure 3.2 Velocities Discretization on a D3Q19 Lattice Model .....	12
Figure 3.3 Velocities Discretization on a D3Q27 Lattice Model .....	12
Figure 3.4 Distribution Functions after the streaming step.....	19
Figure 3.5 Example of an Octree Lattice Structure .....	21
Figure 3.6 Scanned Propeller Blade.....	25
Figure 3.7 Complete Hexacopter Model in SOLIDWORKS .....	26
Figure 3.8 Virtual Wind Tunnel (Top View).....	28
Figure 3.9 Virtual Wind Tunnel (Left View).....	29
Figure 3.10 Rotational direction of each rotor in the Hexacopter .....	30
Figure 3.11 Domain Structure at t=0 sec .....	32
Figure 3.12 Domain Structure at t=3 sec .....	33
Figure 4.1 Vorticity distribution of airflow field.....	34
Figure 4.2 Wingtip Vortex Structure (a) Isometric view (b) Top view .....	35
Figure 4.3 Planar Downwash Airflow Field Area (1 m above the ground).....	36
Figure 4.4 Volumetric velocity field ( $0 < \text{Velocity} < 50 \text{ ms}^{-1}$ ).....	38
Figure 4.5 Distribution of V-y against different flight speeds and flight heights on a side plane ( $-2 < V-y < 0$ ) .....	41
Figure 4.6 The penetrable area A1 Change Trends .....	42
Figure 4.7 The Coverage Area A2 Change Trends.....	43

## LIST OF SYMBOLS, ABBREVIATIONS AND ACRONYMS

UAV	Unmanned Aerial Vehicle
LBM	Lattice Boltzmann Method
RSM	Reynolds Stress Models
SST	Shear Stress Transport Model
LGA	Lattice Gas Automata
PDF	Probability Distribution Function
SRT	Single-Relaxation Time
MRT	Multiple-Relaxation Time
WMLES	Wall-Modeled Large Eddy Simulation
PDAF	Planar Downwash Airflow Field
$\Omega$	Collision Operator
$\delta$	Kronecker delta
$\mathcal{G}_{\alpha\beta}$	Strain-rate Tensor

## ABSTRACT

Multirotor Unmanned Aerial Vehicles (UAVs) as agricultural spraying drones have now become an integral part of the modern agricultural system. They are being used for spraying on the crops to protect the plants from different types of pests. When spray is distributed on the crops, it flows away from the target because of the wind field being created around the UAV. The downwash effect produced by the UAV significantly influences the spray deposition on crops. The downwash airfield generated by the hexacopter brings droplets to the crops, increasing the droplets' deposition on the crops. Lattice Boltzmann Method was applied using CFD package XFlow to study the downwash field created by the hexacopter. The primary focus of the research is the downwash airflow field generated by the hexacopter that affects the motion distribution of droplets released from the sprayer at different flight speeds and altitudes. Previous research is limited to downwash effects on a drone with a wheelbase of 1000 mm. In this study, the downwash effect on a hexacopter drone with a spraying capacity of 30L and a wheelbase of 1900 mm is studied. We compared the results of our larger-wheelbase UAV with existing benchmarks. The UAV showed enhanced performance, achieving coverage and penetrable areas approximately double those of the benchmark. Based upon the results, the optimum flight height and flight velocity for spraying operation are 3 m and  $4 \text{ ms}^{-1}$  respectively under the condition of coverage and penetrable area.

# CHAPTER 1: INTRODUCTION

## 1.1 Background

Agriculture is an essential economic activity of humans around the globe which is providing food and fiber for the survival of people on the earth. In the recent ten years, the field of agriculture has gone through a remarkable transformation with the introduction of new technologies. One such technology that has gained significant importance in agriculture is the introduction of Unmanned Aerial Vehicles. Agricultural UAVs are mostly equipped with cameras, sensors and data collection devices to aid in the management of different types of crops. Sprayer drones contain a medicine kit attached with the UAVs used for spraying on the crops which act as a medicine against pests for different types of crops.

Conventional methods of spraying the crops are time consuming and expensive methods in agricultural methods. Also, they don't provide the level of accuracy required for spraying on the crops. UAVs provide most effective spraying method with the rapid spraying activity on the crops.[1] With the advancement in agricultural drones, the newer drones in the market now provide the drones with larger medicine kits for the spraying activity. With their small size and advanced remote features, they have gained much importance in a small time in the region of Asia. [2]

Apart from spraying, UAVs offer other advantages as well. It gathers high quality resolution images for the crops which enables farmers to monitor the growth and areas of high concerns for the crops. With the addition of specialized sensors, UAVs can capture multispectral data which can reveal information about crop stress and pests' infestations. Through this information of early detection, farmers can take proactive measures against these and can minimize the yield losses.

## **1.2 Problem Statement**

Multicopter Unmanned Aerial Vehicles (UAVs) as agriculture drones have become an integral part of modern agriculture. They are being used for spraying on the crops to protect the plants from different types of pests. When the spray is distributed on the crops, it flows away from the target because of the wind field. The focus of the research is on the impact of downwash and windward airflow on the distribution of droplets released from the sprayer.

## **1.3 Research Aims**

The purpose of the study is to simulate the downwash effect produced by the Hexacopter UAV when it is performing the spraying operation at different flight speeds and altitudes. The LBM approach, utilizing the commercial CFD package XFlow, is employed to model the downwash effect of the Hexacopter UAV.

## **1.4 Significance of Study**

The research will contribute in enhancing the efficiency of agricultural drones while spraying. By analyzing the downwash effect at various flight speeds and flight altitudes, spray distribution on the crops can be optimized. Moreover, this study contribute to the growing application of LBM for complex fluid dynamics problems using DS Simulia XFlow.

## **CHAPTER 2: LITERATURE REVIEW.**

### **2.1 Agricultural UAVs in Farming**

Recently, spraying on the crops using sprayer UAVs has gained a significant importance in the field of agriculture. Conventional Methods of spraying were time consuming and less efficient. UAVs provide efficient and effective ways of spraying crops. Through modern UAVs, farmers could get information about pest infestations in the crops field. With the Early Detection, farmers can take proactive measures against them and can minimize the yield losses.

Manned Aerial Vehicles, used for spraying especially for large cropping area, are less common in Asian countries when compared with the United States. In the last decade, the Unmanned Aerial Vehicles have gained much importance in the Asian countries especially China, Japan and South Korea.[3] UAVs have got some advantages over manned aerial vehicles like they can perform at lower altitude with greater automatic controls and more maneuverability options with the drift caused by downwash effect remains area of high concern.[4]

### **2.2 Simulation Tools**

The traditional CFD solvers use the Navier-Stokes equations to solve the fluid domains. These solvers are generally mesh based and require time consuming meshing process. In order to make the meshing process simpler and easier, the research mostly opt for simpler geometries to avoid meshing errors and convergence issues. The quality of solution for a CFD problem greatly depends upon the mesh of the fluid domain. Different meshes of equivalent sizes generate different solutions. So, one must be careful with the type and size of the mesh. Also, the moving geometry can't be handled in a simpler manner as they change the shape of the fluid area when they start moving. Although there are meshing methods to handle moving geometries, but they require time consuming meshing process.[5]



The accuracy and reliability of solutions in Computational Fluid Dynamics (CFD) are significantly influenced by the mesh used to discretize the fluid domain. A mesh, which consists of a network of nodes and elements, serves as the foundation for numerical simulations by dividing the physical space into discrete cells. The quality of the CFD solution is intrinsically linked to the mesh's characteristics, including its type, size, and refinement.

**Mesh Type:** The choice of mesh type—whether structured, unstructured, or hybrid—affects how well the mesh conforms to the geometry of the fluid domain. Structured meshes, which use a regular grid pattern, can be efficient and easy to handle but may struggle with complex geometries. Unstructured meshes, on the other hand, are more flexible and can adapt to complex shapes but may introduce additional computational overhead. Hybrid meshes combine aspects of both types to balance accuracy and efficiency.

**Mesh Size:** The size of the mesh elements, or cells, plays a crucial role in determining the solution's precision. Finer meshes, with smaller cells, can capture more detailed features of the flow, such as boundary layers, vortices, and localized phenomena. However, finer meshes also demand more computational resources and time to solve. Conversely, coarser meshes may not resolve these details accurately, leading to less precise results. Therefore, selecting an appropriate mesh size involves a trade-off between computational cost and solution accuracy.

**Mesh Refinement:** In CFD simulations, mesh refinement is often used to improve solution quality in specific regions of interest. For example, near boundaries, interfaces, or regions with high gradients, finer mesh elements can enhance the accuracy of the solution. Adaptive mesh refinement techniques dynamically adjust the mesh resolution based on the evolving flow features during the simulation, ensuring that critical areas receive appropriate resolution while optimizing overall computational efficiency.

**Impact on Solution Quality:** Different meshes of equivalent sizes can yield varying results due to differences in how they capture flow features and interactions. Inaccurate or inadequate meshing can lead to numerical errors, convergence issues, and unreliable

results. It is essential to conduct mesh sensitivity analyses to assess how changes in mesh type and size affect the solution. This process helps in determining the optimal mesh configuration that provides a balance between accuracy and computational efficiency.

Turbulence Modeling has always remained a challenge in CFD. Almost all the practical engineering problems are turbulent; therefore, it is necessary to correctly model the turbulence. Numerous turbulence models have been developed to compute the Reynolds-Averaged Navier-Stokes equations, commonly known as RANS turbulence models. These encompass the Spalart-Allmaras,  $k$ - $\omega$  ( $k - \omega$ ), Reynolds Stress Models (RSM),  $k$ - $\epsilon$  ( $k - \epsilon$ ), and the Shear Stress Transport Model (SST).[6] These are the empirical turbulence models and are dependent on large number of constants. Careful calibration is required to correctly model the turbulence. Turbulence Model has a great effect on the product design as it generates uncertainties when design goes through the important changes. In 1964, an intermediate category of turbulence models was first proposed known as Large Eddy Simulation (LES). LES provides an intermediate solution between RANS and DNS (Direct Numerical Solution). It acts as a balance between accuracy and computational cost by explicitly simulating large scale turbulence.[7]

### **2.3 Lattice Boltzmann Method in Fluid Dynamics**

Over the past few decades, there has been significant development in particle-based methods. These approaches have advanced considerably, reflecting the growing interest and progress in this field. The Lattice Boltzmann Method, among particle-based methods, is a computational method used to simulate fluid flows. Typically, particle-based methods are employed to address fluid flow problems involving complicated geometries and boundary conditions. These methods are particularly valuable when dealing with complex and irregular flow domains, as they can efficiently handle the detailed and different aspects of the fluid's behavior within such environments.

In recent years, particle-based methods have risen in prominence, surpassing traditional approaches like finite difference, finite volume, and finite element methods. This shift is due to their superior ability to handle complex fluid dynamics problems, particularly those

involving intricate geometry and boundary conditions. Unlike conventional methods, which may struggle with irregular or highly detailed flow domains, particle-based approaches offer greater flexibility and accuracy, making them more effective for modern computational fluid dynamics applications. Unlike different CFD methodologies which solve conservation equations numerically, LBM represents the behavior of particles on a lattice structure, and it includes collision and propagation steps. In the collision phase, particles engage with one another and adjust their velocities based on collision rules that are informed by the macroscopic behavior of the particles, such as those described by the Navier-Stokes equations. In the subsequent propagation phase, particles travel to adjacent nodes within the lattice structure, updating their positions accordingly.[8]

Lattice Boltzmann Method Approach has gained popularity in Computational Fluid Dynamics methods for the reason that it can solve irregular geometries with complex boundary conditions which makes it suitable to solve complex fluid flow domains. Moreover, LBM can handle fluids with High Reynolds Number making it a suitable method to solve turbulent flows. LBM has also introduced adaptive refinement of grids which is used to capture the fine details at various points of interest. Like, it generates fine lattice grid structure near the moving bodies and coarse structure away from the bodies. Also, Fluid Structure Interaction problems can be simulated using LBM approach.[9]

In Computational Fluid Dynamics, LBM approach treats fluid as a collection of discrete particles which move along specific lattice grid directions. The fluid field is divided into a lattice structure comprising of nodes. Each node is defined with a discrete set of velocities. These discrete sets of velocities form a rectangular lattice structure. D2Q9 and D3Q27 are common lattice structures for 2D and 3D computational fluid domains respectively. Once the domain is discretized, particles are transferred from one node to another at each time step, following predefined discrete velocities. This process is referred to as the propagation step. After this comes the collision step in which distribution functions collide with each other and interaction of particles takes place in between them. The collision step takes according to collision rules and is a crucial step in approximating macroscopic fluid behavior.[10]

While applying boundary conditions, a critical step in CFD, LBM offers great flexibility because of its discrete nature. Macroscopic properties like density and velocities are calculated from the distribution functions which are then used to calculate other properties of fluid such as pressure and stresses. LBM simulations are parallelized because of the lattice-based computations which makes it to utilize efficient use of modern computing resources.[11]

## **2.4 XFlow as a CFD Approach**

In recent years, we have observed that researchers now prefer LBM method over conventional numerical methods. The LBM approach varies significantly from numerical methods based on the incompressible Navier-Stokes equations in several aspects. LBM calculates the fluid domain using a lattice structure, whereas the Navier-Stokes equations are formulated in vector form and are not dependent on any specific coordinates or grid configuration. In the Lattice Boltzmann Method, the convective terms are linear, whereas in the Navier-Stokes equations, these terms are non-linear. In the LBM method, boundary conditions within the fluid domain are represented by particle distribution functions. Both LBM and traditional methods demand meticulous handling of boundary conditions when dealing with complex geometries.[12]

XFlow CFD software from Next Limit Technologies employs the Lattice Boltzmann Method and features a unique, fully Lagrangian particle-based kinetic methodology. XFlow features an innovative collision operator scheme that enhances both order and stability. The octree lattice scheme introduced in XFlow efficiently manages dynamic geometries with its adaptive refinement feature. XFlow utilizes the D3Q27 lattice structure, which provides the highest number of discrete velocities for a fluid domain. XFlow employs a Wall-Modeled Large Eddy Simulation (WMLES) for turbulence modeling and near-wall treatment, delivering advanced capabilities in turbulence prediction. [13]

## **2.5 Previous Studies**

The CFD simulation of a quad-rotor drone, utilizing the LBM approach and the XFlow CFD package, is presented in [14]. Syma X8C quadcopter UAV Model is utilized for this

effort. Among the advantages of using XFlow is the removal of time taking meshing process that we see in traditional N-S equations. In contrast to the volumetric meshing process in traditional Navier Stokes Computational Fluid Dynamics, LBM approach utilizes an orthogonal lattice structure. In this lattice structure, the mesh size at each refinement level is halved compared to the above level. So, the resolution at each refinement level is expressed by the formula  $\frac{x}{2^n}$ , and 'n' is taken as a positive integer. [14] has compared the two resolution cases in XFlow; Fixed Resolution Case and Adaptive Resolution Case. And have concluded that Adaptive case generates the best results providing balance between accuracy and computational cost. Fixed Resolution case is however less efficient and provides the best results only with the finer grids consuming high computational resources.

The airflow field is crucial for effective spraying on the crops field. A numerical simulation of the airflow field from a six-rotor agricultural UAV is detailed in [15]. The airflow field at various heights and various flight speeds was simulated using the commercial LBM code package XFlow. A three-dimensional optical scanner was used to model clockwise and anticlockwise rotors. Disregarding the drone's body, the numerical investigation of the airflow field focused solely on the rotors was performed. A total of eleven cases were considered for the experiment. It was concluded that, to optimize pesticide spraying, flight speeds should be kept under 4 m/s to prevent the airflow wake from lifting off the ground. Also, [15] highlighted that factors such as wind conditions and crop canopy play a crucial role, suggesting that future research should address these variables.

The impact of various factors such as flight speed, altitude, horizontal and vertical wind speeds, and UAV's workload on the downwash airflow field has been examined in [16]. Coverage and penetrable area were taken as assessing criteria for studying the effects of these parameters on the downwash airflow field. In this study, LBM Model D3Q27 is used to distribute velocity on each cell. DJI M600 is used to study the effect of multiple factors on spraying operation. [16] has concluded that altitude of 2-3m and speed of 4 m/s are the perfect parameter when considering coverage and penetrable area as the evaluating criteria for spraying. At the same time, UAVs perform optimally with crosswind speeds of up to 3

m/s Speeds exceeding 3 m/s result in significant lateral drift of the airflow, which becomes a serious factor in reducing the droplet deposition on the crops. Reducing the workload negatively impacts droplet deposition by diminishing the effectiveness of the deposition process.

The analysis of spray distributions from a quad-rotor drone at different flight speeds has been investigated in [17]. The downwash airflow field for a quad-rotor drone was simulated using the Lattice Boltzmann Method. The study concentrated on the behavior of droplets at various flight speeds and UAV's heights during spraying operations, simulated the airflow field using the LBM approach, and validated the results against experimental data from a wind tunnel. Since the wind tunnel involves low-speed flow, the XFlow package, which utilizes the LBM approach, was employed for the numerical simulation of the airflow field. [17] has concluded that flight height and speed are the leading factors in droplet deposition. Meanwhile, the placement of the spray nozzles has minimal influence on both drift and droplet distribution. The results presented in [17] could provide proper technical support to the farmers who have started using multi rotor sprayer drones for the crops. The paper has proposed considering more parameters like Froude numbers to generate more precise results.

## CHAPTER 3: METHODOLOGY

### 3.1 Lattice Boltzmann Method

Among particle-based methods, the Lattice Boltzmann Method addresses many of the limitations found in conventional CFD approaches. The meshing process is eliminated, and the simulation operates on a lattice arranged in an octree structure. The Lattice Boltzmann Method was first introduced as an enhancement to Lattice Gas Automata (LGA) to reduce statistical noise and achieve improved Galilean invariance.[18] Due to its strong link with kinetic theory, the Lattice Boltzmann Method is capable of modeling intricate physical phenomena. Recent advancements have significantly improved physical consistency in models for multiphase and compressible flows.[19]

#### 3.1.1 Lattice Scheme

Particle based methods, like LGA and LBM, use spatial discretization known as lattice for computational fluid dynamics. Unlike traditional methods that rely on grid-based discretization, these techniques utilize a lattice structure to represent the fluid domain.

In these methods, the computational domain is divided into a regular lattice grid where each lattice site represents a point in space. The fluid's properties and dynamics are then modeled based on this lattice framework. The lattice structure essentially divides the domain into discrete cells, each of which interacts with its neighboring cells according to predefined rules or equations.

The Lattice Gas Automaton (LGA) method operates by simulating the fluid as a collection of particles that move and collide on a lattice grid. Each particle's behavior is governed by local rules that mimic the physical processes of fluid flow. As these particles propagate and interact, they collectively produce macroscopic fluid behavior.

The term "DnQm" is commonly used to describe the dimension of the problem and the number of velocity directions. Here, "n" indicates the number of dimensions, while "m" represents the number of possible velocity directions in the model.[20]

D2Q9 is the most common lattice scheme for a two-dimensional model. Figure 3.1 shows the velocity discretization on a D2Q9 lattice scheme.

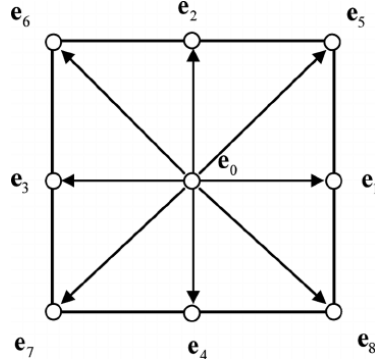


**Figure 3.1 Velocities discretization on a D2Q9 lattice scheme**

It involves 9 velocity vectors and are defined as:

$$e_i = \begin{cases} (0, 0) & i = 0 \\ (1, 0), (0, 1), (-1, 0), (0, -1) & i = 1, 2, 3, 4 \\ (1, 1), (-1, 1), (-1, -1), (1, -1) & i = 5, 6, 7, 8 \end{cases} \quad (3.1)$$

In three dimensional models, the lattice schemes are D3Q19 and D3Q27 lattice models. The most commonly used lattice scheme is D3Q19. Figure 3.2 shows the D3Q19 lattice scheme. It involves 19 velocity vectors and are defined as:

$$e_i = \begin{cases} (0, 0, 0) & i = 0 \\ (\pm 1, 0, 0), (0, \pm 1, 0), (0, 0, \pm 1) & i = 1, 2, \dots, 6 \\ (\pm 1, \pm 1, 0), (\pm 1, 0, \pm 1), (0, \pm 1, \pm 1) & i = 7, 8, \dots, 18 \end{cases} \quad (3.2)$$



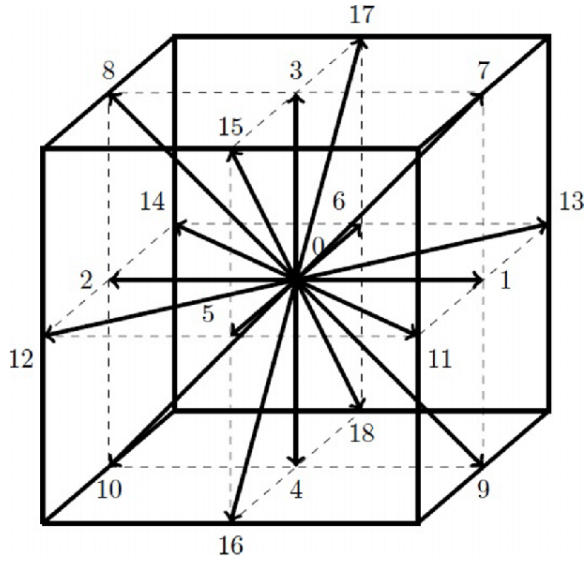


**Figure 3.2 Velocities Discretization on a D3Q19 Lattice Model**

Figure 3.3 shows the velocity discretization on a D3Q27 model. It involves 27 velocity vectors and are defined as:[21]

$$e_i = \begin{cases} (0, 0, 0) & i = 0 \\ (\pm 1, 0, 0), (0, \pm 1, 0), (0, 0, \pm 1) & i = 1, 2, \dots, 6 \\ (\pm 1, \pm 1, 0), (\pm 1, 0, \pm 1), (0, \pm 1, \pm 1) & i = 7, 8, \dots, 18 \\ (\pm 1, \pm 1, \pm 1) & i = 19, 20, \dots, 26 \end{cases} \quad (3.3)$$

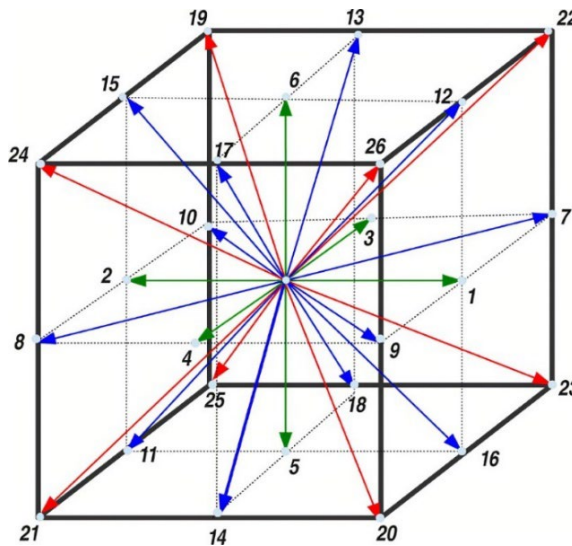


**Figure 3.3 Velocities Discretization on a D3Q27 Lattice Model**

### Figure 3.3 Velocities discretization on a D3Q27 lattice model

#### 3.1.2 Propagate-Collide Scheme

All LBM models share a common feature: their time-stepping approach follows a propagate-collide scheme. After discretization of domain, particles propagate from one node to another. The propagation step generates a fixed time step  $dt$  and establishes a discrete array of velocities ( $e_i$ , where  $i = 1, 2, \dots, b$ ). The set of velocities generate a lattice structure. Probability distribution functions (PDFs)  $f_i(r, t)$  are accumulated at each individual lattice site  $b$ . [22]

The Boltzmann transport equation is expressed using a discrete set of velocities as:

$$\frac{\partial f_i}{\partial t} + e_i \cdot \nabla f_i = \Omega_i, i = 1, 2, \dots, b. \quad (3.4)$$

where  $\Omega_i$  calculates the post collision state, known as collision operator, keeping mass and linear momentum conserved. The lattice representation of equation 3.1 is written as:

$$f_i(r + e_i, t + dt) = f_i(r, t) + \Omega_i(f_1, \dots, f_b), i = 1, \dots, b. \quad (3.5)$$

The collision operator plays a crucial role in simulating most physical phenomena by defining how particle distributions interact and evolve over time. It effectively captures the essential dynamics of collisions and interactions within the system. It plays a critical role in numerical stability of the system.[23]

In the continuum Boltzmann equation, macroscopic variables are obtained by calculating the statistical moments of the probability distribution functions as:

$$\rho = \frac{1}{b} \sum_{i=1}^b n_i \quad (3.6)$$

$$\rho v = \frac{1}{b} \sum_{i=1}^b n_i e_i \quad (3.7)$$

The zero-order moment reflects the overall density of the system, whereas the first-order moment provides information about the momentum distributed across the three spatial dimensions.

In most models, the collision operator is designed to simulate the process of probability distribution functions (PDFs) gradually reaching an equilibrium state. This relaxation process ensures that the system evolves towards a stable distribution. A prevalent method for achieving this is the single-relaxation time (SRT) model, which employs the Bhatnagar-Gross-Krook (BGK) approximation.[24]:

$$\Omega_i^{BGK} = \frac{1}{\tau} (f_i^{eq} - f_i) \quad (3.8)$$

Here  $\tau$  denotes the relaxation time and  $f_i^{eq}$  represents the local equilibrium function.

Applying the Chapman-Enskog expansion to the LBM equation establishes a relationship between the kinematic viscosity and the relaxation time, [25]providing the following relation:

$$v = c_s^2 \left( \tau - \frac{1}{2} \right) \quad (3.9)$$

where  $c_s$  represents the speed of the sound. This relaxation at the collision step models the fluid kinematic viscosity while controlling the response to the equilibrium.

The local equilibrium function, which is based on the Maxwell-Boltzmann distribution, maintains consistency with the macroscopic variables of the pre-collision state, while

keeping mass and momentum conserved during the process. It relies exclusively on the macroscopic characteristics of the flow and is commonly expressed as:

$$f_i^{eq} = \rho \omega_i \left( 1 + \frac{e_{i\alpha} u_\alpha}{c_s^2} + \frac{u_\alpha u_\beta}{2c_s^2} \left( \frac{e_{i\alpha} e_{i\beta}}{c_s^2} - \delta_{\alpha\beta} \right) \right) \quad (3.10)$$

where  $u$  represents the macroscopic velocity,  $\delta$  is for the Kronecker delta and the  $\omega$  denotes the weighting constants introduced to retain the isotropy. The indices  $\alpha$  and  $\beta$  represent the different spatial components of the vectors in the equation, and Einstein's summation convention is applied to the repeated indices. The indices  $\alpha$  and  $\beta$  identify the different spatial directions in the equation, with Einstein's summation convention applied to any indices that are repeated.

The Chapman-Enskog expansion is utilized to demonstrate how the resulting scheme models the hydrodynamic regime for flows with low Mach numbers. [26] Recent research has highlighted parallels between the LBM approach and various artificial compressibility methods. [27] It is possible to design an artificial compressibility method that closely mirrors the LBM approach at the procedural level.

To address the limitations of the single-relaxation time collision operator, the multiple-relaxation time collision operator was developed. This method processes the collision interactions in momentum space rather than in velocity space. [28] Further work was done for D2Q9 lattice scheme and D3Q19 by [29]. Research has shown that multiple-relaxation time models offer improved accuracy over single-relaxation time models. This enhancement arises because multiple relaxation times are used independently to achieve better stability and performance. [30]

Similarly to equations 3.6 and 3.7, the general form for the raw moment  $\mu$  and the PDF  $f$ , can be written as:

$$\mu_{x^k y^l z^m} = \sum_{i=1}^b f_i e_{ix}^k e_{iy}^l e_{iz}^m \quad (3.11)$$

here  $k$ ,  $l$ , and  $m$  denote the moment orders in the  $x$ ,  $y$ , and  $z$  directions respectively. Therefore, the total order of the raw moment will become  $k + l + m$ . The raw moment is denoted as  $\mu_i$  as a raw moment  $\mu_{x^k y^l z^m}$  of combination  $(k, l, m)$ , the equation between the probability distribution function and the raw moments can be expressed in the following form of matrix:

$$\mu_i = M_{ij} f_j \quad (3.12)$$

$M_{ij}$  represents the transformation matrix. The raw moments  $\mu_i$  are limited to the number of discrete velocities.

Similarly to equation 3.8, the ‘‘multiple-relaxation time collision operator’’  $\Omega^{MRT}$  is determined through relaxation in momentum space as below:

$$\Omega_i^{MRT} = -M_{ij}^{-1} \hat{S}_{ij} (\mu_i^{eq} - \mu_i) \quad (3.13)$$

where  $\hat{S}_{ij}$  represent the diagonal relaxation matrix, and  $\mu_i^{eq}$  represents the raw moment at a stable stage. After obtaining the  $\mu_i$  after the collision has occurred, the probability distribution function can be generated from the:

$$f_j = M_{ij}^{-1} \mu_i \quad (3.14)$$

For example, the moment vector for D2Q9 lattice scheme can be defined as:

$$\mu = (\mu_0, \mu_1, \dots, \mu_8)^T = (\rho, e, \epsilon, j_x, q_x, j_y, q_y, p_{xx}, p_{yy})^T \quad (3.15)$$

here  $e$  denotes the energy kinetic,  $\rho$  represents the density,  $\epsilon$  is linked to kinetic energy square,  $j_x$  and  $j_y$  are the momentum components in  $x$  and  $y$  directions,  $q_x$  and  $q_y$  represent

the energy components, and  $p_{xx}$  and  $p_{yy}$  are the traceless viscous stress tensor in a symmetric manner in corresponding  $x$  and  $y$  directions.

Utilizing the Gram-Schmidt orthogonalization methodology used in [29] and using equation 3.11, the raw moments contribution for each  $f_i$  can be written as

$$\rho |i = |e_i|^0 = 1 \quad (3.16)$$

$$e |i = -4 |e_i|^0 + 3(e_{i,x}^2 + e_{i,y}^2) \quad (3.17)$$

$$\epsilon |i = 4 |e_i|^0 - 21/2(e_{i,x}^2 + e_{i,y}^2) + 9/2 (e_{i,x}^2 + e_{i,y}^2)^2 \quad (3.18)$$

$$j_x |i = e_{i,x} \quad (3.19)$$

$$q_x |i = e_{i,x}[-5|e_i|^0 + 3(e_{i,x}^2 + e_{i,y}^2)] \quad (3.20)$$

$$j_y |i = e_{i,y} \quad (3.21)$$

$$q_y |i = e_{i,y}[-5|e_i|^0 + 3(e_{i,x}^2 + e_{i,y}^2)] \quad (3.22)$$

$$p_{xx} |i = (e_{i,x}^2 - e_{i,y}^2)\rho \quad (3.23)$$

$$p_{xy} |i = e_{i,x}e_{i,y}/\rho \quad (3.24)$$

So, the transformation matrix  $M$  will be as:

$$M = \begin{pmatrix} \rho |i \\ e |i \\ \epsilon |i \\ j_x |i \\ q_x |i \\ j_y |i \\ q_y |i \\ p_{xx} |i \\ p_{xy} |i \end{pmatrix} = \begin{pmatrix} 1 & 1 & 1 & 1 & 1 & 1 & 1 & 1 & 1 \\ -4 & -1 & -1 & -1 & -1 & 2 & 2 & 2 & 2 \\ 4 & -2 & -2 & -2 & -2 & 1 & 1 & 1 & 1 \\ 0 & 1 & 0 & -1 & 0 & 1 & -1 & -1 & 1 \\ 0 & -2 & 0 & 2 & 0 & 1 & -1 & -1 & 1 \\ 0 & 0 & 1 & 0 & -1 & 1 & 1 & -1 & -1 \\ 0 & 0 & -2 & 0 & 2 & 1 & 1 & -1 & -1 \\ 0 & 1 & -1 & 1 & -1 & 0 & 0 & 0 & 0 \\ 0 & 0 & 0 & 0 & 0 & 1 & -1 & 1 & -1 \end{pmatrix} \quad (3.25)$$

$S^{ij} = \text{diag}(s_0, s_1, s_2, s_3, s_4, s_5, s_6, s_7, s_8)$  is the “relaxation matrix” in a diagonal manner. The kinematic and bulk viscosity ( $\nu$  and  $\mu$  respectively) are represented with the other parameters in the following manner:

$$\nu = c_s^2 \left( \frac{1}{s_7} - \frac{1}{2} \right) = c_s^2 \left( \frac{1}{s_8} - \frac{1}{2} \right), \mu = \frac{5 - 9c_s^2}{9} \left( \frac{1}{s_1} - \frac{1}{2} \right) \quad (3.26)$$

For stability, each value of  $s_i$  must lie between 0 and 2.

Finally, utilizing the transformation matrix against the probability distribution function of equation 3.10 at the stable position, the raw moments will become:

$$e^{eq} = -2\rho + 3(j_x^2 + j_y^2)$$

$$\epsilon^{eq} = \rho - 3(j_x^2 + j_y^2)$$

$$q_x^{eq} = -j_x$$

$$q_y^{eq} = -j_y \quad (3.27)$$

$$p_{xx}^{eq} = j_x^2 - j_y^2$$

$$p_{xy}^{eq} = j_x j_y$$

### 3.1.3 Boundary Conditions

Boundary conditions are essential pre-processing features that have a major impact on the accuracy and effectiveness of numerical simulations. They are critical for the stability and accuracy of the simulation. Boundary conditions establish the necessary values for the unknown probability distribution functions in lattice Boltzmann method that emerge after the streaming step in simulations.

Figure 3.4 shows the boundary condition on a wall on a D2Q9 lattice structure. Lattice points are positioned on the left side of the wall to facilitate the implementation of the wall boundary condition. The unknown PDFs,  $f_1$ ,  $f_5$  and  $f_8$ , varies with the wall locations and directions. In Figure 3.4, the boundary conditions will only impact on these unknown functions.

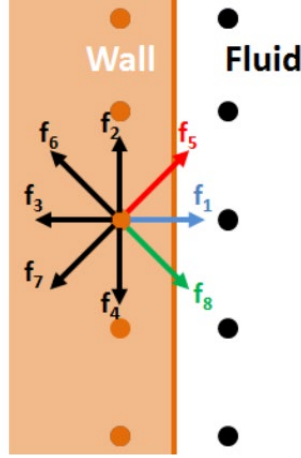


**Figure 3.4 Distribution Functions after the streaming step**

The crucial boundary conditions at inlet and outlets in CFD are velocity and pressure as these parameters can be analyzed easily. The initial formulations for velocity and pressure boundary conditions in the Lattice Boltzmann method were proposed by [31].

The method involves creating a linear system based on the principles of mass and momentum conservation. This system will determine the values of the unknown probability distribution functions, along with  $\rho$  (when applying velocity boundary conditions) or  $u$  (when applying pressure boundary conditions). In the Figure 3.4, after rearranging moments equations, the system of equations will become:

$$\begin{aligned}
 f_1 + f_5 + f_8 &= \rho - (f_0 + f_2 + f_4 + f_3 + f_6 + f_7) \\
 f_1 + f_5 + f_8 &= \rho u + f_3 + f_6 + f_7 \\
 f_5 - f_8 &= \rho v + f_2 + f_4 - f_6 + f_7
 \end{aligned}
 \tag{3.28}$$



To calculate the velocity, a boundary condition at inlet is applied on the nodes at the left side of the Figure 3.4, so we will get the equation:

$$f_1 - f_1^{eq} = f_3 - f_3^{eq} \quad (3.29)$$

Solving this system of equations, the values for unknown PDFs will become:

$$f_1 = \frac{2}{3}\rho u$$

$$f_5 = f_7 - \frac{1}{2}(f_2 - f_4) + \frac{1}{6}\rho u + \frac{1}{2}\rho v \quad (3.30)$$

$$f_8 = f_6 - \frac{1}{2}(f_2 - f_4) + \frac{1}{6}\rho u + \frac{1}{2}\rho v$$

For boundary condition of velocity, the equations will give:

$$\rho = \frac{1}{1-v} [f_0 + f_2 + f_4 + 2(f_3 + f_6 + f_7)] \quad (3.31)$$

For boundary condition of pressure, at  $v=0$ , the value of  $u$  will become:

$$u = 1 - \frac{[f_0 + f_2 + f_4 + 2(f_3 + f_6 + f_7)]}{\rho} \quad (3.32)$$

The reflections may occur at inlets and outlets due to the unsteady and compressible nature of the Lattice Boltzmann Method.

### 3.2 XFlow as an Advanced CFD Approach

The CFD software XFlow utilizes the Lattice Boltzmann Method and provides fully Lagrangian, particle-based kinetic methodology. XFlow offers a unique collision operator scheme that increase order and approaches towards a stable solution. The octree lattice

scheme featured in XFlow efficiently manages dynamic geometries with its adaptive refinement feature. The lattice structure featured in XFlow is D3Q27 which offers maximum number of discrete velocities for a fluid domain. XFlow employs a Wall-Modeled Large Eddy Simulation (WMLES) for turbulence modeling and near-wall treatment, delivering advanced capabilities in turbulence prediction.

### 3.2.1 Octree Lattice Structure

XFlow's pre-processor creates the octree lattice framework according to the geometry, lattice resolution values for different geometry shapes and for far-field resolution.

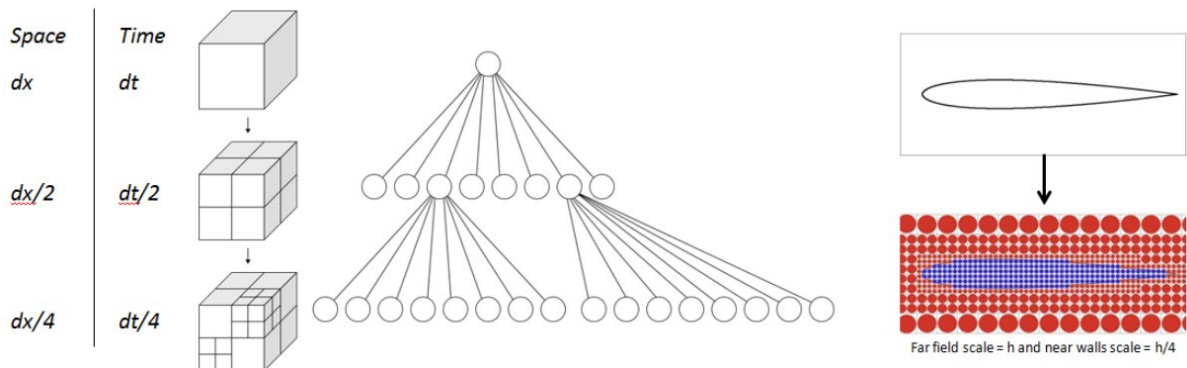


**Figure 3.5 Example of an Octree Lattice Structure**

From Figure 3.5, Each level addresses a scale that is half the size of the previous level, thereby constructing an octree structure. The local time step model in XFlow adjusts the time step according to each lattice size within the fluid domain. Additionally, the initial lattice structure is updated during simulations to accommodate any moving geometries within the fluid domain. A refinement algorithm in XFlow is defined as adaptive refinement which gives an option to redefine the lattice structure for moving geometries at each time step.

### 3.2.2 Lattice Boltzmann Method using Central-Moment

XFlow employs a multiple relaxation time (MRT) approach for its collision operator. Unlike conventional MRT methods used in traditional Lattice Boltzmann implementations, XFlow defines its scattering operator in central momentum space. The following describes the central moments:

$$\tilde{\mu}_{x^k y^l z^m} = \sum_i^N f_i (e_{ix} - u_x)^k (e_{iy} - u_y)^l (e_{iz} - u_z)^m \quad (3.33)$$

where  $u_x$ ,  $u_y$ , and  $u_z$  denote the components of the overall average velocity in  $x$ ,  $y$  and  $z$  direction respectively. Employing macroscopic velocity rather than discrete particle velocities leads to substantial improvements in Galilean invariance and numerical stability. [32]. Central moments are calculated first, and then the inverse transformation matrix is used to determine the values for the probability distributions. [33]

XFlow employs Large Eddy Simulations (LES) to model turbulence, incorporating an additional term known as turbulent eddy viscosity for sub-grid turbulence representation. To ensure precise modeling of turbulence near walls, XFlow utilizes the Wall-Adapting Local Eddy (WALE) viscosity model within its LES framework. This model provides a consistent local eddy viscosity and effectively captures the behavior of turbulence in close proximity to walls.

The utilization of turbulence modeling in XFlow is as follows:

$$v_t = \Delta_f^2 \frac{(G_{\alpha\beta}^d G_{\alpha\beta}^d)^{3/2}}{(S_{\alpha\beta} S_{\alpha\beta})^{5/2} + (G_{\alpha\beta}^d G_{\alpha\beta}^d)^{5/4}} \quad (3.34)$$

$$S_{\alpha\beta} = \frac{g_{\alpha\beta} + g_{\beta\alpha}}{2} \quad (3.35)$$

$$G_{\alpha\beta}^d = \frac{1}{2}(g_{\alpha\beta}^2 + g_{\beta\alpha}^2) - \frac{1}{3}\delta_{\alpha\beta} g_{\gamma\gamma}^2 \quad (3.36)$$

$$g_{\alpha\beta} = \frac{\partial u_{\alpha}}{\partial x_{\beta}} \quad (3.37)$$

Where  $\Delta_f = C_w \Delta_x$ ,  $S$  represents the strain tensor associated with the resolved scales.. The value of  $C_w$  is mostly taken near to 0.33.  $g_{\alpha\beta}$  is the strain rate tensor. In finite element methods, the value of the strain rate tensor depends on the neighboring nodes. Similarly, in finite volume methods, the strain rate tensor is also influenced by the surrounding nodes. Accessing memory to compute neighboring node values can be highly inefficient compared to Lattice Boltzmann Methods (LBM). XFlow's lattice structure, however, is well-suited for the Large Eddy Simulation (LES) turbulence model. This is because the LES model benefits from cells with a proportional aspect ratio, which aligns with the isotropic nature of turbulence outside the boundary layer.

### 3.2.3 Turbulence Modeling

XFlow employs the Wall-Modeled LES (WMLES) approach to simulate the boundary layer and near-wall regions. Given the isotropic nature of the lattice structure, resolving the boundary layer with high accuracy would typically demand a large number of elements. To address this challenge, XFlow utilizes a generalized law of the wall.

The isotropic nature of the lattice structure used in XFlow presents a unique challenge when resolving boundary layers. In LES, the resolution of turbulence near the wall often requires a very fine mesh to accurately capture the small-scale turbulent structures. For a high-fidelity simulation, this would mean employing a large number of mesh elements, which can significantly increase computational demands and processing time.

To overcome the challenges posed by the isotropic lattice structure, XFlow employs a generalized law of the wall. This approach simplifies the modeling of turbulence near the wall by using empirical and theoretical formulations that represent the behavior of the boundary layer without the need for an excessively fine mesh. The generalized law of the wall provides a practical and efficient means of capturing the essential features of the

boundary layer turbulence, including the velocity profile and frictional effects, without resorting to an impractically dense mesh.

The generalized law of the wall enhances the simulation of near-wall turbulence by providing a reliable model that accounts for the effects of both adverse and favorable pressure gradients, ensuring that the boundary layer is modeled with sufficient precision.

This approach effectively models the boundary layer, allowing for accurate simulation while minimizing the need for excessively fine discretization. [34] This technique addresses the influences of pressure gradients, whether adverse or favorable.

$$\frac{U}{u_c} = \frac{U_1 + U_2}{u_c} = \frac{u_\tau U_1}{u_c u_\tau} + \frac{u_p U_2}{u_c u_p} \quad (3.38)$$

$$= \frac{\tau_w u_\tau}{\rho u_\tau^2 u_c} f_1 \left( y + \frac{u_\tau}{u_c} \right) + \frac{dp_w/dx}{|dp_w/dx|} \frac{u_p}{u_c} f_2 \left( y + \frac{u_p}{u_c} \right) \quad (3.39)$$

$$y^+ = \frac{u_c y}{\nu} \quad (3.40)$$

$$u_c = u_\tau + u_p \quad (3.41)$$

$$u_\tau = \sqrt{|\tau_w|/\rho} \quad (3.42)$$

$$u_p = \left( \frac{\nu}{\rho} \left| \frac{dp_w}{dx} \right| \right)^{1/3} \quad (3.43)$$

$y$  is the perpendicular distance against the wall,  $x$  is the tangential direction of the local flow along the wall,  $u_\tau$  refer to the friction velocity,  $\tau_w$  indicates the turbulent wall shear stress,  $\frac{dp_w}{dx}$  is the wall pressure gradient, the characteristic velocity associated with the adverse wall pressure gradient is represented as  $u_p$ .

### 3.3 Scanning of Propeller Blade

3D scanners are used to capture the complex geometries i.e. profile of propellers as used by [15]. To accurately capture the geometry of the propeller for our six-rotor agricultural drone, a 3D scanner was employed. The scanning process was conducted using VX Elements, a sophisticated software suite designed for high-precision 3D scanning. This technology allowed us to create a detailed digital model of the propeller's complex geometry.

Once the scanning process was complete, the acquired 3D data was processed and converted into a part file using Geomagic Design X Software. Geomagic Design X is a powerful tool for converting scanned data into CAD models, enabling precise engineering analysis and design modifications. This conversion facilitated the integration of the propeller geometry into our drone's design and simulation workflows, ensuring accuracy in performance analysis.

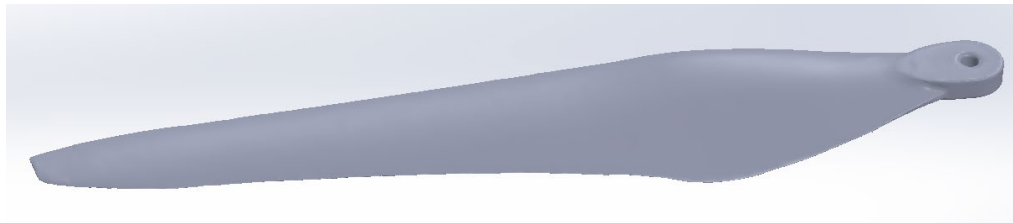


**Figure 3.6 Scanned Propeller Blade**

### 3.4 Development of Hexa-copter Geometry

The modeling of the hexacopter's geometry was carried out using SolidWorks, a comprehensive computer-aided design (CAD) software. This process involved creating a detailed 3D model of the hexacopter, starting with the main body. The body was designed based on precise measurements obtained from the actual drone, ensuring that the model accurately reflects the physical dimensions and structural characteristics of the real hexacopter.

In addition to modeling the body, the propellers were incorporated into the design. The propeller geometry was based on data obtained from a 3D scan of the actual propellers. This scanning process provided highly accurate and detailed information about the propeller's shape and dimensions. Using SolidWorks, the scanned data was converted into a digital model, which was then integrated into the overall hexacopter design.

By combining the CAD model of the body with the accurately scanned propeller geometry, the final model of the hexacopter was created. This comprehensive modeling approach ensured that both the structural and aerodynamic features of the hexacopter were represented with high fidelity, facilitating precise simulations and analyses for performance evaluation.

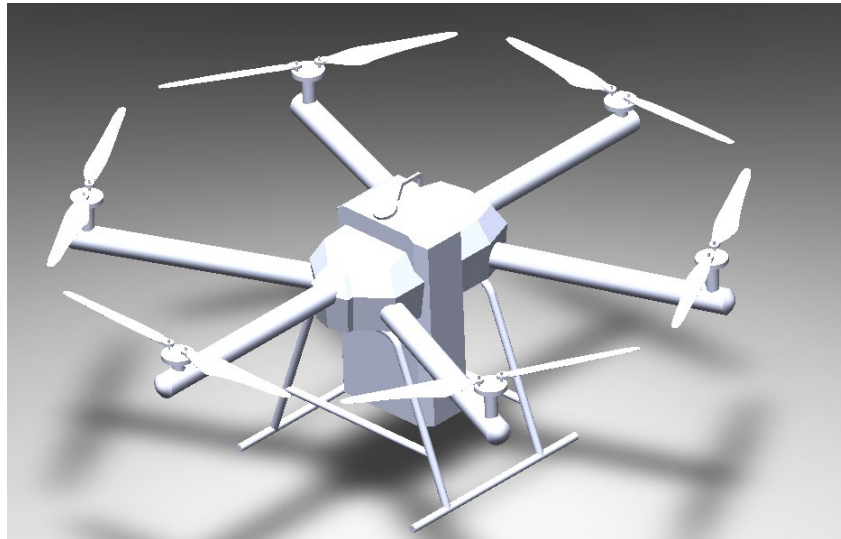


**Figure 3.7 Complete Hexacopter Model in SOLIDWORKS**

### **3.5 Downwash Analysis utilizing XFlow**

The Lattice Boltzmann Method (LBM) was employed through the CFD software XFlow to analyze the downwash field produced by the hexacopter. This computational approach allows for a detailed examination of the airflow dynamics and its interaction with the environment, specifically focusing on the downwash effect.

The downwash field, created by the hexacopter's rotors, plays a critical role in the agricultural spraying process. As the hexacopter flies and generates downwash airflow, it propels droplets towards the crops. This process is crucial for ensuring effective application of the spray, as the downwash carries the droplets directly onto the plant surfaces. Consequently, the droplets' deposition on the crops is enhanced, which significantly improves both the coverage and penetration of the spray.

By analyzing the downwash area produced by the hexacopter, the effectiveness of the spray deposition can be evaluated. This evaluation involves assessing how well the droplets are distributed over the crops and how effectively they penetrate into the plant canopy. The insights gained from studying the downwash field provide valuable information for optimizing spray operations, ensuring that the maximum amount of droplets reaches the target areas on the crops.

### *3.5.1 Environment*

A **single-phase flow model** was employed to investigate the downwash patterns generated by the hexacopter sprayer drone within its operational fluid domain. This model simplifies the analysis by focusing solely on the behavior of the airflow without accounting for additional complexities such as multi-phase interactions. By utilizing this approach, we can effectively study how the airflow behaves as it interacts with the drone's components and the surrounding environment.

The **k-epsilon turbulence model** was selected for this study to capture the effects of turbulence within the fluid domain. This model is well-suited for simulating turbulent flows in engineering applications due to its balance between accuracy and computational efficiency. The k-epsilon model provides a framework for predicting turbulence characteristics, such as the intensity and distribution of eddies and vortices, which are crucial for understanding how the downwash affects the spray dispersion.

A **virtual wind tunnel** was used as the fluid domain for the simulation, with the setup including a ground wall to represent the terrain over which the hexacopter operates. This virtual wind tunnel setup provides a controlled environment that mirrors real-world



conditions, allowing for accurate analysis of the downwash patterns. The domain was dimensioned at **50 x 32 x 6 meters**, providing ample space to capture the full extent of the downwash effect and its interaction with the ground and surrounding air.

Figures 3.8 and 3.9 illustrate the configuration of the virtual wind tunnel and the direction of flight for the hexacopter. These figures provide visual context for the setup, showing how the airflow is simulated and how the direction of the drone's flight influences the downwash patterns. The representation in these figures helps to understand the spatial arrangement and the flow dynamics within the simulated environment, which are critical for analyzing the effectiveness of the spray distribution.

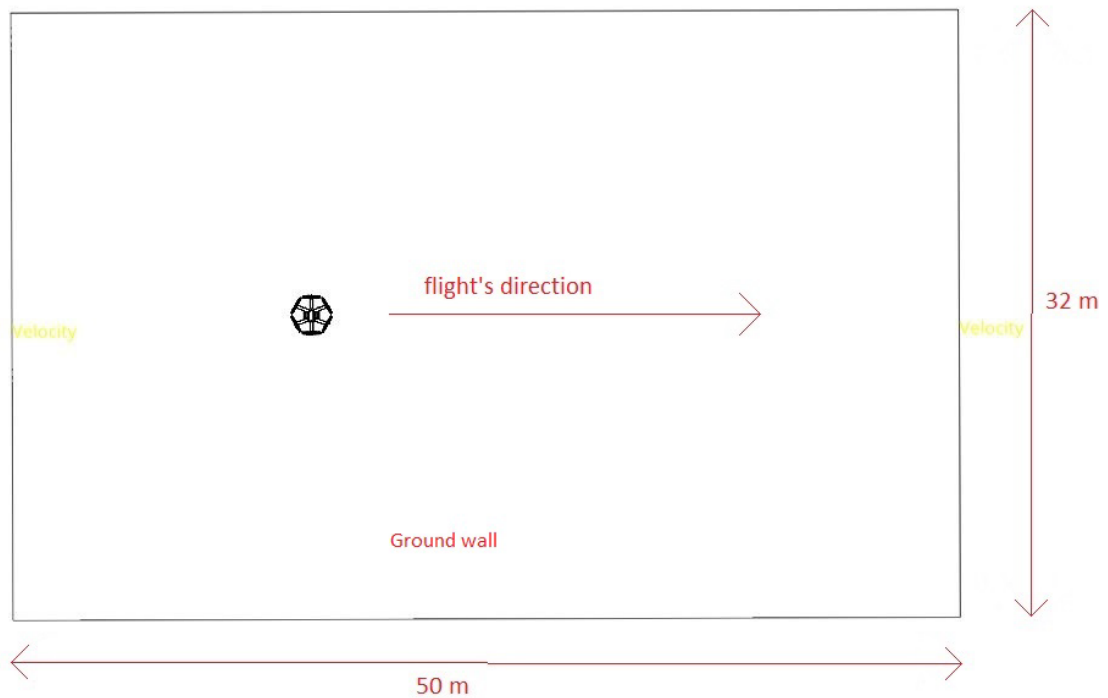


**Figure 3.8 Virtual Wind Tunnel (Top View)**

Figure 3.8 shows the top view of the virtual wind tunnel while Figure 3.9 illustrates the left view of the fluid's domain. The ground wall is turned on with a gravitational pull of  $-9.8 \text{ ms}^{-2}$ . **Standard air conditions** were applied throughout the fluid domain and around the UAV, which involves assuming typical atmospheric parameters such as air density and viscosity. This standardization helps in maintaining consistency and reliability in the

simulation results, ensuring that the observed downwash patterns and spray distribution align with expected real-world behavior under normal atmospheric conditions.

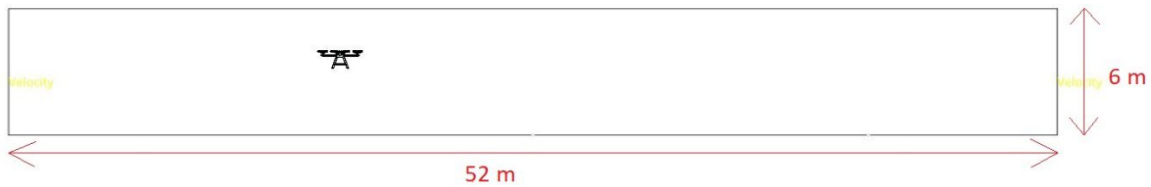


**Figure 3.9 Virtual Wind Tunnel (Left View)**

### 3.5.2 Geometry

The rotors of the UAV were configured to reflect their real-world operational setup. Specifically, three of the rotors were set to rotate in a clockwise (CW) direction, while the remaining three rotors were configured to rotate in an anticlockwise (ACW) direction. This configuration mirrors the typical arrangement found in hexacopter UAVs, where alternating rotor directions help to balance and stabilize the drone. The CW and ACW rotations ensure proper torque compensation and contribute to the overall aerodynamic stability of the hexacopter during its flight.

Figure 3.8 shows the rotors configuration in the geometry. The rotational velocity for each rotor was taken as 3868 RPMs. So, the angular law defined for the rotational velocity in y-direction was  $3868 \cdot 6t$  degrees (equivalent to 3868 RPM). The boundary condition for the rotors was set to "enforced," which implies that the simulation enforces specific constraints or conditions on the rotor surfaces. This could involve defining how the rotors interact with the fluid flow, such as specifying the velocity or force applied to the rotors to simulate their dynamic behavior accurately. In contrast, the UAV body was assigned a "fixed" boundary condition. This means that the UAV body is treated as stationary, with no movement or deformation allowed in response to the fluid flow. This condition ensures that the body of the UAV remains stationary throughout the simulation, providing a stable reference for studying the downwash and its effects.

By applying these boundary conditions, the simulation effectively captures the different roles and interactions of the UAV's components with the surrounding airflow, allowing for an accurate analysis of the downwash field and spray distribution.



**Figure 3.10 Rotational direction of each rotor in the Hexacopter**

### *3.5.3 Pre-Processing*

The time step in a computational simulation is a crucial parameter that determines the frequency at which the simulation updates its calculations. In this study, each simulation was conducted with a time step of 0.0005 seconds. This choice of time step is a balance between computational accuracy and resource constraints.

A smaller time step generally enhances the precision of the simulation by allowing more frequent updates of the state of the fluid dynamics. This leads to a more detailed and accurate representation of transient phenomena, such as the dynamic behavior of the downwash effect generated by the hexacopter. However, smaller time steps also demand significantly more computational power and memory, as the simulation has to process a larger number of updates within the same overall time frame.

In this research, a time step of 0.0005 seconds was selected to ensure a high level of temporal resolution while remaining within the limits of available computational resources. This time step allows for a detailed analysis of the interactions between the hexacopter's downwash and the surrounding fluid, contributing to a more accurate assessment of spray deposition patterns and their impact on crop coverage. Despite the constraints, this configuration aimed to achieve a balance between computational feasibility and simulation accuracy.

**Table 1 - Lattice resolutions and adaptive wake refinement threshold values**

No.	Region	Resolution/ Threshold
1	Around Rotors	0.0125
2	UAV Body	0.1
3	Far Field	0.2
4	Wake Resolution	0.025
5	Wake Refinement Threshold	0.00001

Adaptive refinement was taken as the refinement algorithm for the each simulation. Adaptive refinement provides more accurate results for the moving geometries when compared with fixed refinement algorithm.[35] Figure 11 and 12 shows the domain structure at two different time intervals.

Fixed refinement involves maintaining a consistent grid resolution across the entire simulation domain. In this approach, the mesh size is uniform throughout the simulation, regardless of variations in fluid flow characteristics or areas of particular interest. Fixed refinement offers simplicity and predictability due to its uniform nature, but it may not be the most efficient or accurate method, especially in regions where finer details are crucial, such as near boundary layers or in areas with significant gradients.

On the other hand, adaptive refinement dynamically adjusts the mesh resolution based on the needs of the simulation. This method increases the mesh resolution in regions where higher detail is required, such as areas with complex flow features, high gradients, or significant changes in the flow field. Conversely, the mesh is coarsened in regions where the flow is relatively uniform or less complex. The primary advantage of adaptive refinement is its ability to enhance accuracy by focusing computational resources on areas of high variability while optimizing resource use by refining the mesh only where necessary. This results in a more detailed simulation in critical areas while managing computational costs effectively.

In XFlow, adaptive refinement is utilized to automatically adjust the grid resolution based on the evolving characteristics of the flow. This capability allows the simulation to capture complex flow features with high accuracy and efficiency, focusing computational effort where it is most needed while maintaining overall resource efficiency.

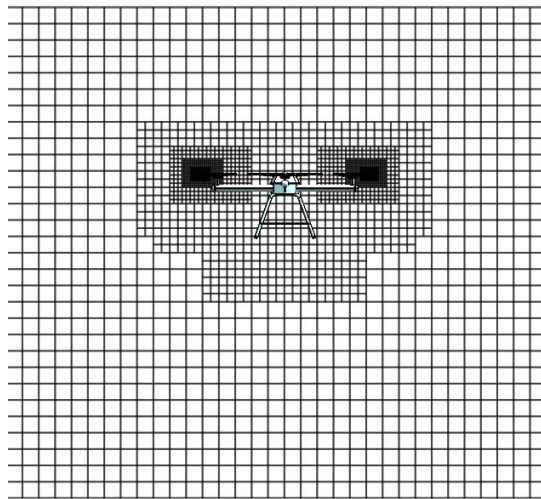


**Figure 3.11 Domain Structure at t=0 sec**

Figure 3.11 shows the domain structure at  $t=0$  sec. The initial domain structure is defined according to the preset values of the lattice resolution of rotors, UAV body and far field conditions. As the simulation progresses, the domain structure changes according to the wake region.

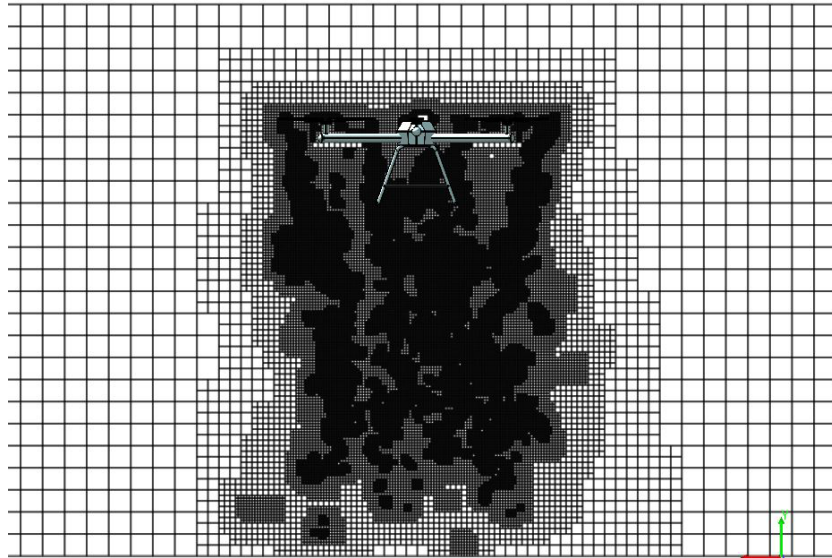


**Figure 3.12 Domain Structure at  $t=3$  sec**

When rotors start moving and produce a downwash airflow field, the structure of the lattice domain changes accordingly. This dynamic interaction necessitates adjustments in the lattice structure of the simulation domain to accurately capture the evolving flow characteristics. Figure 3.12 illustrates the lattice structure of the domain after 3 seconds of simulation. It can be seen in the figure that lattice resolutions have been updated as the wake regions progress downwards. Initially, the lattice domain is set up with a predefined resolution.

However, as the rotors produce downwash airflow, the wake regions created by the rotors start to evolve, and their influence extends throughout the fluid domain. This progression requires the lattice resolution to be adapted to accurately represent the changing flow patterns and wake structures. This adaptive approach ensures that the simulation can accurately model the intricate behavior of the downwash airflow and its effects on the surrounding fluid domain, providing more reliable and detailed results.

## CHAPTER 4: RESULTS AND DISCUSSIONS

### 4.1 Downwash Airflow field

The downwash field generated by the UAV generated a spiral wake vortex near the propellers spreading flow on the ground. Wingtip vortices were formed on the tips of rotors of the UAV as shown in Figure 4.1 and Figure 4.2. A small clearance gap among the rotors caused considerable interference at the wing tip vortex resulting in inter-wing interference. The wing tip vortex generated at each rotor tip induced spiral vortex below the UAV, that appeared 0 m - 0.5 m below it. As the airflow field evolved under the UAV, the vortices of each rotor advanced towards each other causing serious interference and thus destroying the spiral wake vortex structure. The spiral wake vortex, after interference, turned into a turbulent wake as shown in Figure 4.1. The distribution of droplets from the spray onto the crops was primarily influenced by the turbulent wake region. Figure 4.1 illustrates the generation of vortices around the rotors to the turbulent region under the UAV.

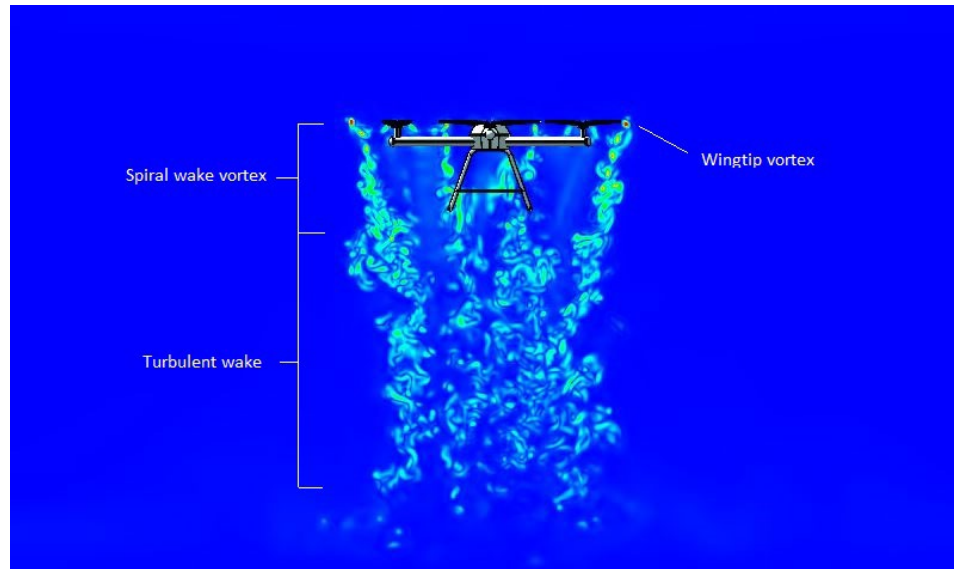


**Figure 4.13 Vorticity distribution of airflow field**

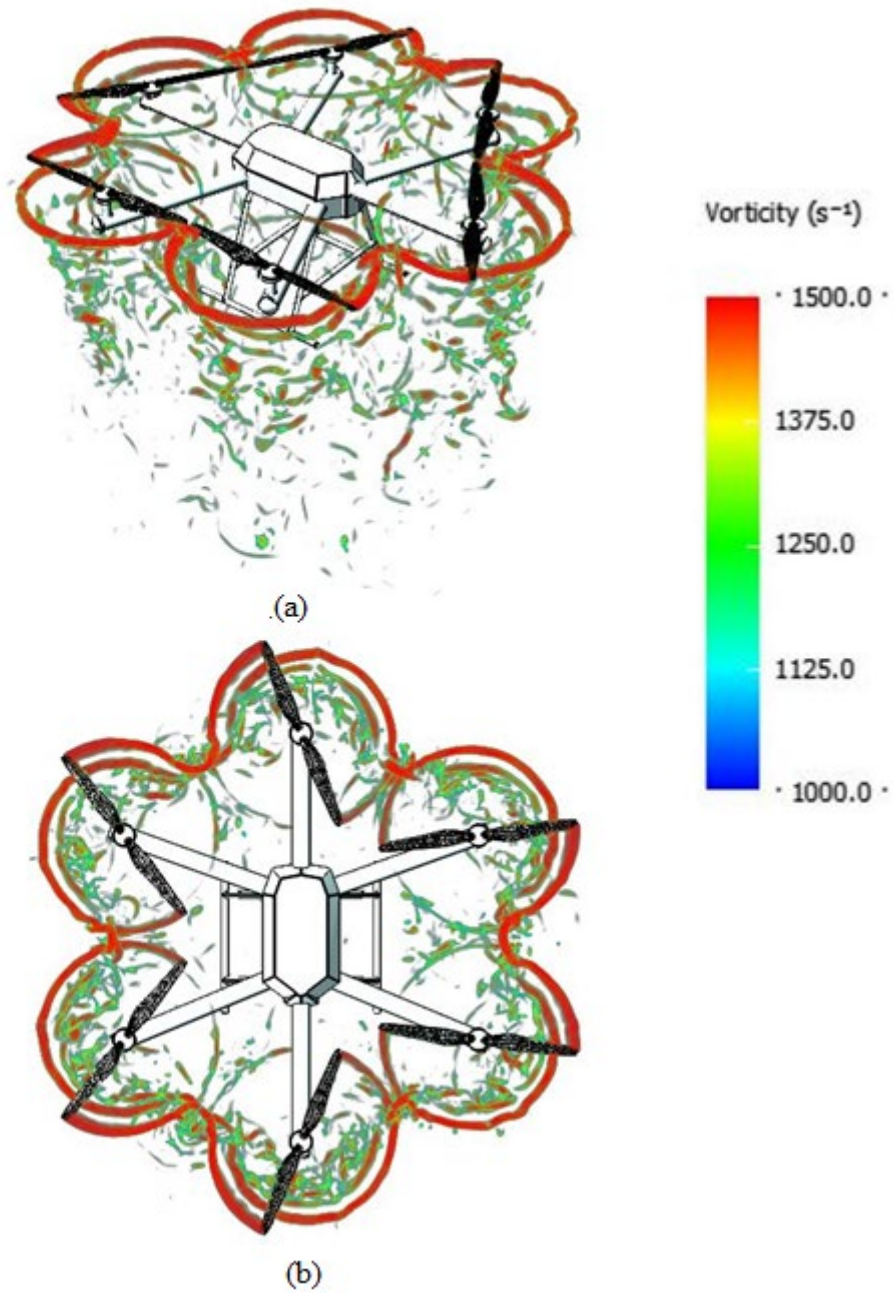
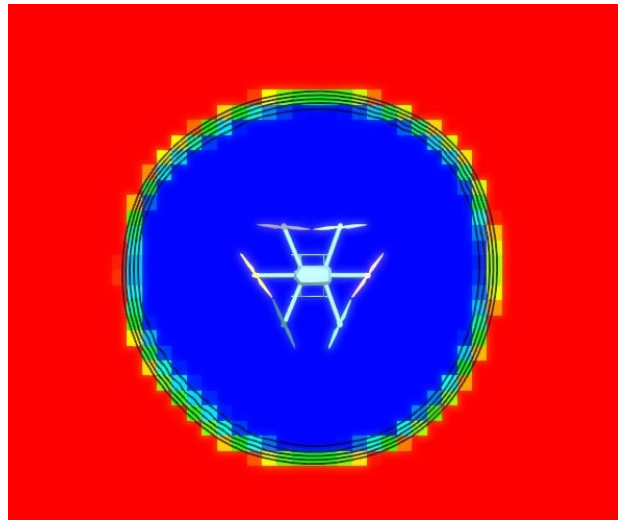


Figure 4.14 Wingtip Vortex Structure (a) Isometric view (b) Top view



## 4.2 Evaluating Index

During the spraying operation on the crops, the vertical velocity  $V_y$  plays an important role in depositing the droplets on the crops. In this study,  $V_y$  has been used as an evaluating index to analyze the distribution of spray by the UAV on the crops at different flight velocities and altitudes. Taking the crop height as 1 m from the ground, the variation of  $V_y$  on the horizontal plane has been studied. The downwash airflow field 1 m above the ground is defined as “planar downwash airflow field” (PDAF). [15]



**Figure 4.15 Planar Downwash Airflow Field Area (1 m above the ground)**

The region covered by the iso-contour ( $V_y < -0.5$  m/s) on the PDAF is the coverage area and is defined as A1. The area covered by the iso-contour ( $V_y < -2.0$  m/s) in the PDAF is the penetrable area and is defined as A2. A1 and A2 are used as evaluating index to study the impact of flight altitude and flight velocities on the spraying distribution by the UAV. [16]

## 4.3 Downwash Airflow field at Various Flight Speeds and Heights

The spray droplets are carried to the crops by the downwash airflow generated by the hexacopter, enhancing their deposition and thus improving their penetration. When flight height and speed increases, the droplet drift increases and droplet deposition decreases.

A parametric study at flight speeds of 1 – 5 ms<sup>-1</sup> was performed to study the airflow field generated by the UAV at the flight heights of 2 m and 3 m. Table 2 shows a parametric study for 10 cases at various flight speeds and flight heights.

**Table 2 Parameters for study of airflow field**

Case No.	Flight Height	Flight Velocity
1	2 m	1 ms <sup>-1</sup>
2	3 m	1 ms <sup>-1</sup>
3	2 m	2 ms <sup>-1</sup>
4	3 m	2 ms <sup>-1</sup>
5	2 m	3 ms <sup>-1</sup>
6	3 m	3 ms <sup>-1</sup>
7	2 m	4 ms <sup>-1</sup>
8	3 m	4 ms <sup>-1</sup>
9	2 m	5 ms <sup>-1</sup>
10	3 m	5 ms <sup>-1</sup>

#### *4.3.1 Volumetric Velocity Field*

Figure 16 illustrates the downwash velocity field produced by the UAV at various flight speeds and altitudes. It was observed that, at a constant height, the backward tilt angle of the downwash airflow field increases with rising velocity. The greatest backward tilt angle

was recorded at a flight speed of 5 m/s and a flight altitude of 3 meters.

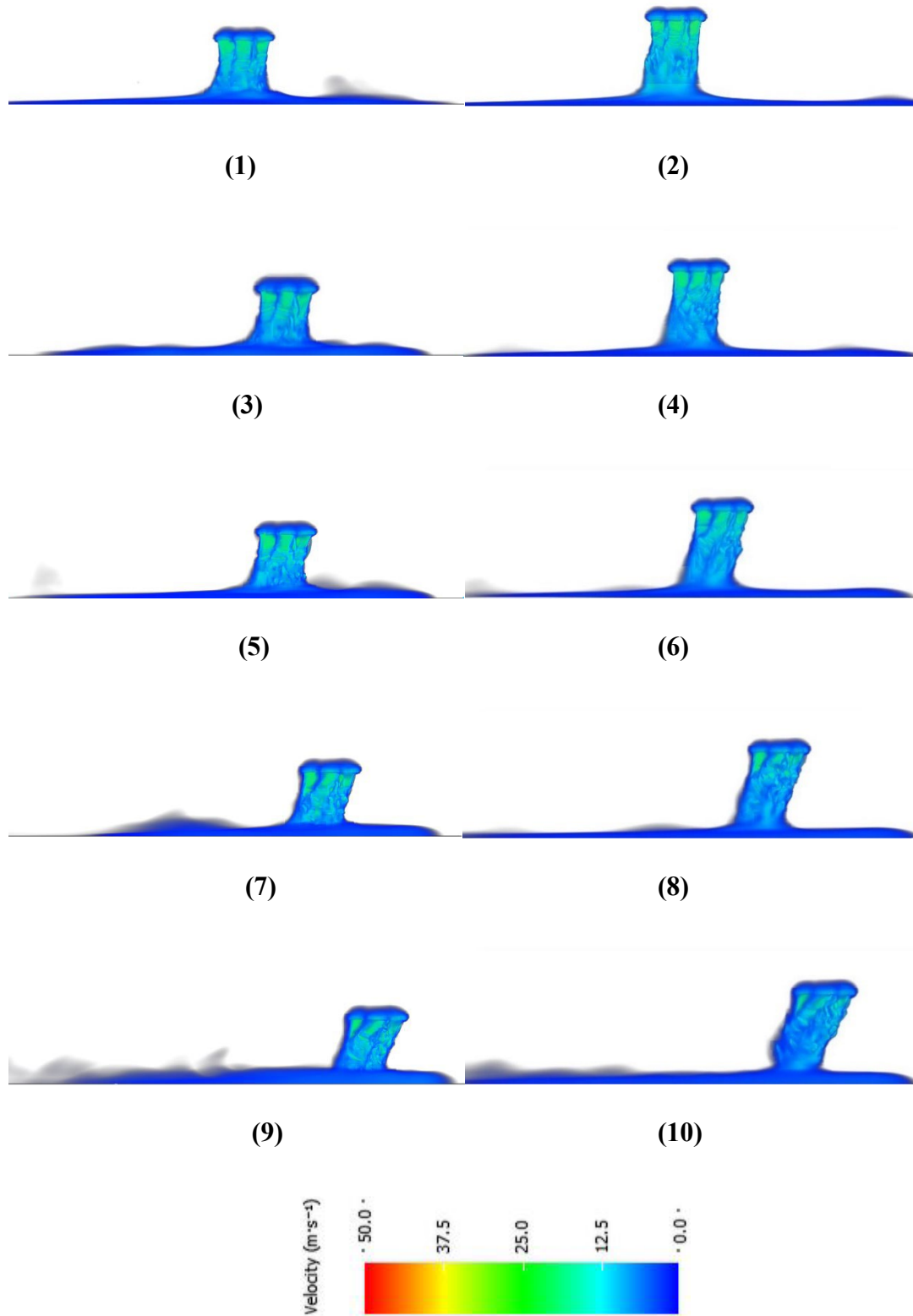


Figure 4.16 Volumetric velocity field ( $0 < \text{Velocity} < 50 \text{ ms}^{-1}$ )

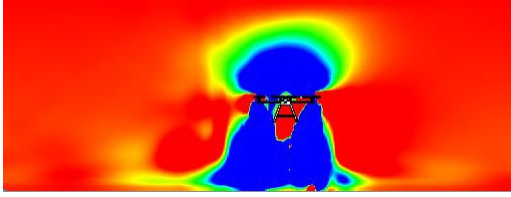
The posterior slope represents the angle of backward tilt of the rotor downwash airflow field during UAV flight. According to Figure 16, this slope grows with higher flight speeds at a constant altitude. The most significant posterior slope is noted at a flight speed of 5 m/s and an altitude of 3 meters. As the posterior slope becomes steeper, droplet deposition tends to decrease.

#### *4.3.2 Distribution of V-y on the PDAF*

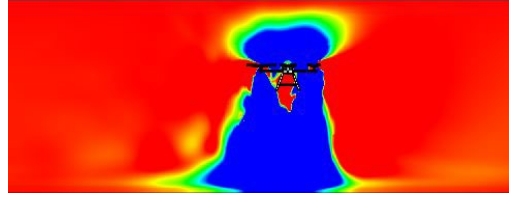
The variation of V-y on the planar downwash field generated by the UAV (1 m above the ground) was taken as the main evaluating index to measure the downwash area generated by the hexacopter. This approach involves analyzing how the vertical velocity component varies across the planar downwash field created by the UAV.

The reason for focusing on V-y at this specific altitude is that it provides a clear indication of how the downwash airflow interacts with the ground and the crops. By examining V-y at 1 meter, we can evaluate how well the hexacopter's downwash airflow distributes spray droplets over the target area. The magnitude and distribution of V-y at this height directly reflect the intensity and reach of the downwash effect, which is crucial for determining the effectiveness of the spraying operation.

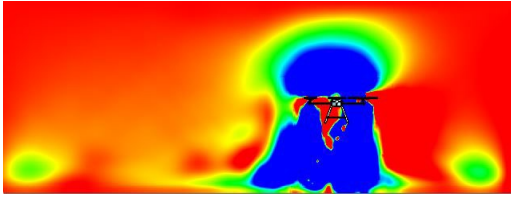
A higher value of V-y indicates a more substantial downward airflow, which can enhance the deposition of spray droplets on the crops. Conversely, lower values of V-y may suggest a weaker downwash effect, potentially leading to reduced coverage and less effective spraying. By systematically analyzing the variations in V-y across the planar field, researchers can quantify the downwash area and assess how different flight speeds, altitudes, and other parameters influence the spray distribution and overall performance of the hexacopter in agricultural applications. This detailed evaluation is essential for optimizing the UAV's spraying capabilities and ensuring efficient crop treatment.



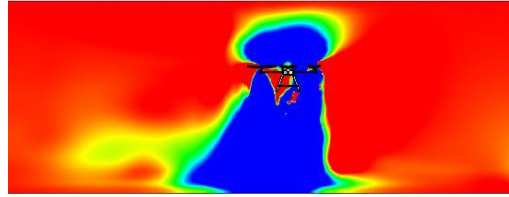
(1)



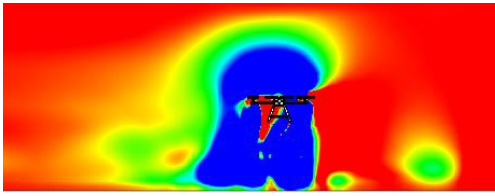
(2)



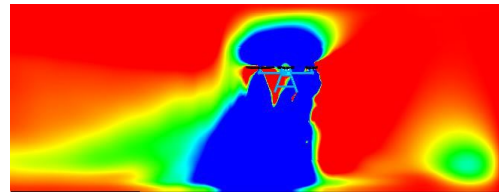
(3)



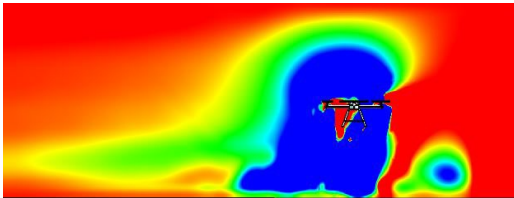
(4)



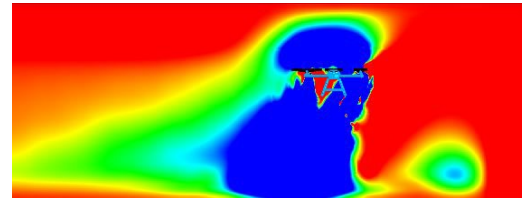
(5)



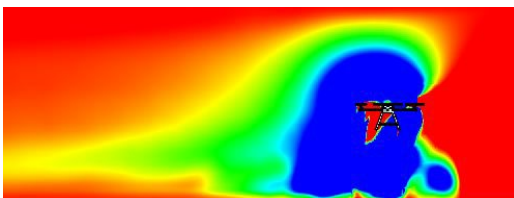
(6)



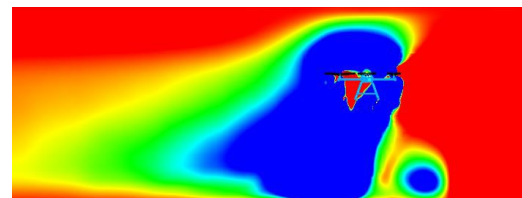
(7)



(8)



(9)



(10)



**Figure 4.17 Distribution of V-y against different flight speeds and flight heights on a side plane ( $-2 < V-y < 0$ )**

#### 4.3.3 The penetrable and coverage area

In agricultural spraying operations, **coverage** and **penetrable area** are critical metrics that assess the effectiveness of spray distribution on crops.

**Coverage** refers to the extent of the area that receives the sprayed droplets. It is a measure of how widely the spray pattern disperses over the crop field. High coverage ensures that a larger portion of the field is exposed to the spray, which is essential for achieving uniform application and effective treatment of the crops.

**Penetrable** area, on the other hand, pertains to the depth or extent to which the spray droplets penetrate the crop canopy. This is particularly important for achieving adequate treatment in dense or tall crops where the spray must reach the lower layers of the foliage. Effective penetration ensures that the spray effectively contacts all parts of the crop, including those that are shielded or less accessible.

The relationship between these metrics and operational parameters such as flight speed and altitude is crucial. For instance, at higher flight velocities and altitudes, the spray droplets experience increased drift due to stronger air currents. This drift can lead to a significant reduction in both the coverage and penetrable area. As droplets are carried away from their intended target, less of the crop field receives the spray, and the ability of the spray to penetrate the crop canopy diminishes.

The penetrable area covered by the iso-contour ( $V-y < - 2.0 \text{ ms}^{-1}$ ) is measured at flight speed of  $1 - 5 \text{ ms}^{-1}$  at flight heights of 2 and 3 m. Figure 18 shows the penetrable area. The

maximum area is observed at a flight speed of 4 ms<sup>-1</sup> and 3 m. A sudden decrease in area is observed at a flight speed of 5 ms<sup>-1</sup> at an altitude of 3 m.

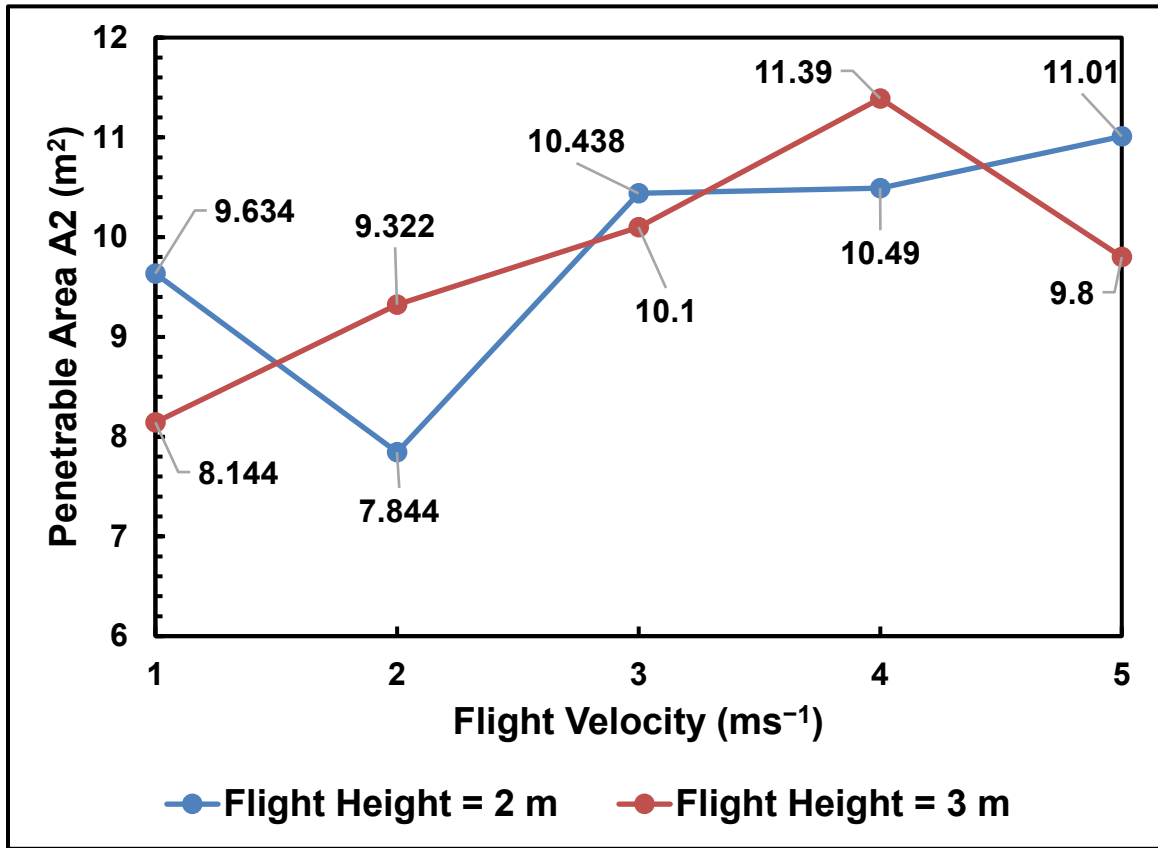
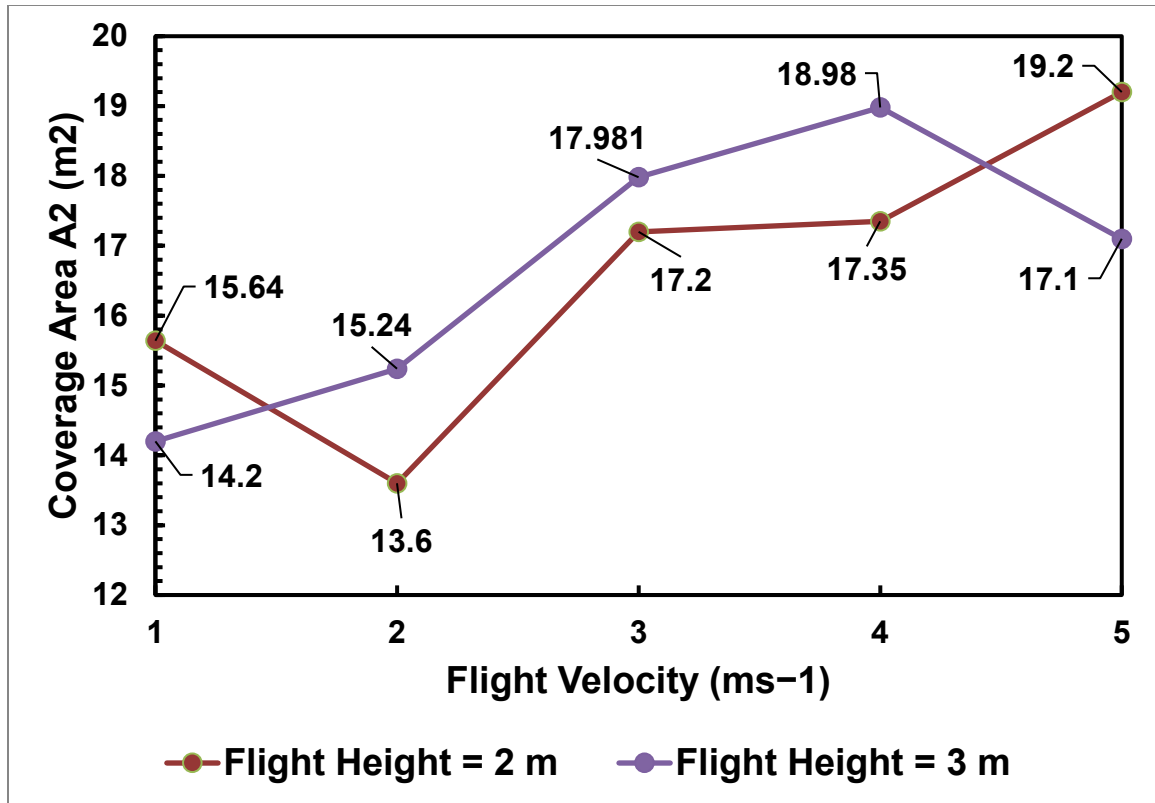


Figure 4.18 The penetrable area A1 Change Trends

The coverage area covered by the iso-contour ( $V_y < -0.5 \text{ ms}^{-1}$ ) is measured at flight speed of 1 – 5 ms<sup>-1</sup> at flight heights of 2 and 3 m. Figure 19 shows the coverage area. The maximum area is observed at a flight speed of 4 ms<sup>-1</sup> and 3 m. A sudden decrease in area is observed at a flight speed of 5 ms<sup>-1</sup> at a flight height of 3 m.

At higher velocities, the force exerted on the droplets by the downwash airflow becomes stronger, causing them to spread out more widely and travel further from the UAV. Similarly, increased altitude exacerbates this effect by allowing more time for the droplets to be influenced by these forces before reaching the crops. The combined effect of higher velocities and greater heights means that the droplets are dispersed over a larger area, reducing the concentration of spray directly reaching the crops.



**Figure 4.19 The Coverage Area A2 Change Trends**

The sudden decrease in coverage and penetrable area at a velocity of 5 ms<sup>-1</sup> and an altitude of 3 m is due to the increase in droplets drift. The droplets drift increases at higher flight velocities and flight altitude and hence lower the spray coverage on the crops.

The increased drift ultimately results in lower spray coverage and effectiveness. The droplets that do manage to settle on the crops may not be uniformly distributed, leading to uneven application and reduced overall efficacy. This underscores the importance of optimizing flight velocity and altitude to minimize drift and enhance the precision and effectiveness of the spraying operation.

We conducted a comparative analysis with the findings of paper [16], which utilized the DJI M600 UAV with a wheelbase of 1130 mm. Our study involved a UAV with a significantly larger wheelbase of 1900 mm. We assessed both UAVs under comparable conditions, specifically focusing on flight heights of 2 and 3 meters and velocities ranging from 1 to 4 m/s.



Our UAV exhibited markedly better performance in all tested scenarios. A key observation was that, while [16] reported a decline in coverage and penetrable areas starting at a flight velocity of 4 m/s, our UAV maintained superior performance with a delay in the onset of decline until a velocity of 5 m/s. This extended efficiency at higher speeds can be attributed to the larger wheelbase of our UAV, which contributes to enhanced aerodynamic stability and improved spray distribution.

Furthermore, the analysis revealed that our UAV achieved coverage and penetrable areas that were nearly twice as large as those reported in [16]. For example, at a flight height of 3 meters and a velocity of 3 m/s, the coverage area in our study was 10.438 m<sup>2</sup>, and the penetrable area was 17.981 m<sup>2</sup>. In contrast, [16] reported coverage and penetrable areas of 4.95 m<sup>2</sup> and 10.02 m<sup>2</sup>, respectively, under the same conditions. This significant increase in area underscores the enhanced efficacy of our UAV in delivering spray coverage and penetration, highlighting the advantages of a larger wheelbase in optimizing performance in agricultural spraying operations.

## CHAPTER:5 CONCLUSION

A three-dimensional model of hexacopter T630 was simulated using Lattice Boltzmann Method utilizing CFD package XFlow. The variation patterns of downwash field generated by the hexacopter at various flight speeds and flight heights. The velocity in y-direction was used as an evaluating index to analyze the downwash airflow field using coverage and penetrable area. The influence of flight speed and height on the sprayer UAV was studied. The results led to the following conclusions:

1. The flight speed has a definite effect on the downwash effect generated by the hexacopter. The angle of the downwash effect's backward tilt increases with higher flight velocities. The coverage and penetrable expand with the increase in the flight velocity. Thus, the downwash area generated by the UAV increases with the addition in the flight velocity until a certain limit. After that, the downwash area starts decreasing with the addition in flight speed. At an altitude of 3 m from the ground, it was observed that the penetrable and coverage area increased significantly with the addition in flight speed. The maximum area was observed at a flight velocity of  $4 \text{ ms}^{-1}$  and it started decreasing at a flight speed of  $5 \text{ ms}^{-1}$ .
2. Like flight speed, the flight altitude has a major impact on the spray deposition on the crops. As the flight height increases, the downwash area increases. But at larger heights, the eddies below the UAV gradually become larger and converge around each other hence decreasing the droplet deposition on the crops. These larger eddies tend to converge and interact more extensively, disrupting the uniformity of the spray pattern. This disruption causes a reduction in the efficiency of droplet deposition, as the spray becomes more dispersed and less concentrated. Consequently, while higher flight altitudes may cover a larger area, they also lead to decreased deposition effectiveness on the crops.
3. At elevated flight velocities, the angle of the posterior slope of the downwash field increases, resulting in a more pronounced backward tilt. This increased tilt adversely affects the spray's ability to settle on the crops, leading to reduced coverage and deposition efficiency. As the flight velocity rises, the downwash

airflow becomes more angled, which contributes to a higher drift of the droplets and less effective delivery to the target area. So based upon the results, the optimum flight height and flight velocity for spraying operation are 3 m and 4 ms<sup>-1</sup> respectively under the condition of coverage and penetrable area.

4. The coverage area variation at different UAV velocities can be explained by the changes in the downwash effect and airflow dynamics. At 2 m/s, the coverage area decreased due to increased turbulence and uneven droplet distribution caused by the unstable interaction between the downwash and forward flight airflow. However, at higher velocities (3 m/s and above), the airflow becomes more stable, reducing turbulence and enhancing droplet dispersion. This leads to a larger and more effective coverage area, with the maximum observed at 5 m/s. Understanding these dynamics is crucial for optimizing UAV flight parameters to achieve efficient and effective spraying operations in agricultural applications.
5. In our study, we compared the performance of our UAV with that of the DJI M600 used in [16]. While it employed a UAV with a 1130 mm wheelbase, our UAV featured a larger 1900 mm wheelbase. We evaluated both UAVs at flight heights of 2 and 3 meters and velocities from 1 to 4 m/s. Our UAV consistently outperformed the DJI M600, showing improved coverage and penetrable areas. Specifically, while [16] observed a decline in performance at 4 m/s, our UAV maintained effectiveness until 5 m/s. Additionally, at a height of 3 meters and 3 m/s velocity, our UAV achieved coverage, and penetrable areas approximately double those of the DJI M600. This indicates that the larger wheelbase of our UAV enhances its performance in terms of spray distribution and efficiency.

## CHAPTER 6: FUTURE WORK AND RECOMMENDATIONS

This thesis has primarily focused on analyzing the downwash effect of a hexacopter and predicting its impact on spray deposition on crops. While this work has provided valuable insights into the behavior of downwash under varying flight speeds and heights, it is inherently limited by its scope.

To build upon these findings, future research should explore the multiphase flow capabilities of XFlow, which would allow for a more comprehensive simulation of the spraying process. The inclusion of multiphase modeling would enable a deeper understanding of how different phases interact and affect the overall efficiency of the spraying operation. However, it is important to note that multiphase simulations require significant computational resources, which was a constraint for the current study.

In addition to expanding the model to include multiphase dynamics, future work should also consider additional factors such as crosswind speed and workload. These factors are crucial for a more accurate simulation of real-world conditions but were not addressed in this study. Although some research has examined these variables, it has typically been limited to small UAVs. Given that this study focuses on a hexacopter with a wheelbase of 1900mm, exploring these factors could provide new insights into the performance of larger UAV systems in agricultural applications.

Furthermore, incorporating advanced algorithms and optimization techniques in the simulation could enhance the accuracy and efficiency of the model. Developing methods to integrate real-time data from operational UAVs could also improve the relevance and applicability of the findings. By addressing these aspects, future research can contribute to more effective and precise agricultural spraying solutions, ultimately benefiting crop management practices and operational efficiency.

## REFERENCES

- [1] D. J. Ruktanonchai *et al.*, “Effect of aerial insecticide spraying on West Nile virus disease-north-central Texas, 2012,” *American Journal of Tropical Medicine and Hygiene*, vol. 91, no. 2, pp. 240–245, 2014, doi: 10.4269/ajtmh.14-0072.
- [2] D. Odido and D. Starovoytova Madara, “Emerging Technologies: Use of Unmanned Aerial Systems in the Realisation of Vision 2030 Goals in the Counties,” 2013. [Online]. Available: [www.ijastnet.com](http://www.ijastnet.com)
- [3] Q. Tang *et al.*, “Effects of application height and crosswind on the crop spraying performance of unmanned helicopters,” *Comput Electron Agric*, vol. 181, Feb. 2021, doi: 10.1016/j.compag.2020.105961.
- [4] C. J. Preftakes, “EXPOSURE AND RISK TO NON-TARGET RECEPTORS FOR AGRICULTURAL SPRAY DRIFT OF FORMULATION TYPES AND ADJUVANTS,” 2017.
- [5] A. Katz and V. Sankaran, “Mesh quality effects on the accuracy of CFD solutions on unstructured meshes,” *J Comput Phys*, vol. 230, no. 20, pp. 7670–7686, 2011, doi: 10.1016/j.jcp.2011.06.023.
- [6] K. Duraisamy, G. Iaccarino, and H. Xiao, “Turbulence Modeling in the Age of Data,” 2018, doi: 10.1146/annurev-fluid-010518.
- [7] Y. Zhiyin, “Large-eddy simulation: Past, present and the future,” Feb. 01, 2015, *Chinese Journal of Aeronautics*. doi: 10.1016/j.cja.2014.12.007.
- [8] R. M. C. So, R. C. K. Leung, E. W. S. Kam, and S. C. Fu, “Progress in the development of a new lattice Boltzmann method,” Aug. 15, 2019, *Elsevier Ltd*. doi: 10.1016/j.compfluid.2019.04.009.
- [9] A. Fakhari and T. Lee, “Finite-difference lattice Boltzmann method with a block-structured adaptive-mesh-refinement technique,” *Phys Rev E Stat Nonlin Soft Matter Phys*, vol. 89, no. 3, Mar. 2014, doi: 10.1103/PhysRevE.89.033310.
- [10] C. K. Aidun and J. R. Clausen, “Lattice-boltzmann method for complex flows,” Jan. 01, 2010. doi: 10.1146/annurev-fluid-121108-145519.
- [11] D. A. Perumal and A. K. Dass, “A Review on the development of lattice Boltzmann computation of macro fluid flows and heat transfer,” Dec. 01, 2015, *Elsevier B.V.* doi: 10.1016/j.aej.2015.07.015.

- [12] D. Yu, R. Mei, L. S. Luo, and W. Shyy, “Viscous flow computations with the method of lattice Boltzmann equation,” Jul. 2003. doi: 10.1016/S0376-0421(03)00003-4.
- [13] M. Chávez-Modena, J. L. Martínez, J. A. Cabello, and E. Ferrer, “Simulations of aerodynamic separated flows using the lattice boltzmann solver XFlow,” *Energies (Basel)*, vol. 13, no. 19, Oct. 2020, doi: 10.3390/en13195146.
- [14] S. E. Thibault, D. Holman, G. Trapani, and S. Garcia, “CFD simulation of a quad-rotor UAV with rotors in motion explicitly modeled using an LBM approach with adaptive refinement,” in *AIAA SciTech Forum - 55th AIAA Aerospace Sciences Meeting*, American Institute of Aeronautics and Astronautics Inc., 2017. doi: 10.2514/6.2017-0583.
- [15] H. Zhang, L. Qi, Y. Wu, E. M. Musiu, Z. Cheng, and P. Wang, “Numerical simulation of airflow field from a six-rotor plant protection drone using lattice Boltzmann method,” *Biosyst Eng*, vol. 197, pp. 336–351, Sep. 2020, doi: 10.1016/j.biosystemseng.2020.07.018.
- [16] L. Wang, M. Xu, Q. Hou, Z. Wang, Y. Lan, and S. Wang, “Numerical verification on influence of multi-feature parameters to the downwash airflow field and operation effect of a six-rotor agricultural UAV in flight,” *Comput Electron Agric*, vol. 190, Nov. 2021, doi: 10.1016/j.compag.2021.106425.
- [17] S. Wen *et al.*, “Numerical analysis and validation of spray distributions disturbed by quad-rotor drone wake at different flight speeds,” *Comput Electron Agric*, vol. 166, Nov. 2019, doi: 10.1016/j.compag.2019.105036.
- [18] G. R. Mcnamara and G. Zanetti, “Use of the Boltzmann Equation to Simulate Lattice-Gas Automata,” vol. 61, doi: 10.1016/j.jcp.1994.05.004.
- [19] A. Gabbana, D. Simeoni, S. Succi, and R. Tripiccone, “Relativistic lattice Boltzmann methods: Theory and applications,” Jun. 03, 2020, *Elsevier B.V.* doi: 10.1016/j.physrep.2020.03.004.
- [20] D. B. Dhuri, S. M. Hanasoge, P. Perlekar, and J. O. A. Robertsson, “Numerical analysis of the lattice Boltzmann method for simulation of linear acoustic waves,” *Phys Rev E*, vol. 95, no. 4, Apr. 2017, doi: 10.1103/PhysRevE.95.043306.
- [21] K. Suga, Y. Kuwata, K. Takashima, and R. Chikasue, “A D3Q27 multiple-relaxation-time lattice Boltzmann method for turbulent flows,” *Computers and Mathematics with Applications*, vol. 69, no. 6, pp. 518–529, Mar. 2015, doi: 10.1016/j.camwa.2015.01.010.
- [22] C. Coreixas, G. Wissocq, B. Chopard, and J. Latt, “Impact of collision models on the physical properties and the stability of lattice Boltzmann methods: Impact of collision models,” *Philosophical Transactions of the Royal Society A*:

*Mathematical, Physical and Engineering Sciences*, vol. 378, no. 2175, Jul. 2020, doi: 10.1098/rsta.2019.0397.

- [23] C. Coreixas, B. Chopard, and J. Latt, “Comprehensive comparison of collision models in the lattice Boltzmann framework: Theoretical investigations,” *Phys Rev E*, vol. 100, no. 3, Sep. 2019, doi: 10.1103/PhysRevE.100.033305.
- [24] L. A. Hegele, K. Mattila, and P. C. Philippi, “Rectangular lattice-boltzmann schemes with BGK-collision operator,” *J Sci Comput*, vol. 56, no. 2, pp. 230–242, Aug. 2013, doi: 10.1007/s10915-012-9672-x.
- [25] Z. Guo and C. Shu, *Lattice Boltzmann Method and Its Applications in Engineering*, vol. Volume 3. WORLD SCIENTIFIC, 2013. doi: doi:10.1142/8806.
- [26] Y. H. Qian, D. D’Humières, and P. Lallemand, “Lattice BGK Models for Navier-Stokes Equation,” *Europhys Lett*, vol. 17, no. 6, p. 479, 1992, doi: 10.1209/0295-5075/17/6/001.
- [27] P. Asinari, T. Ohwada, E. Chiavazzo, and A. F. Di Rienzo, “Link-wise artificial compressibility method,” *J Comput Phys*, vol. 231, no. 15, pp. 5109–5143, Jun. 2012, doi: 10.1016/j.jcp.2012.04.027.
- [28] “Generalized Lattice-Boltzmann Equations,” in *Rarefied Gas Dynamics: Theory and Simulations*, American Institute of Aeronautics and Astronautics, 1994, pp. 450–458. doi: 10.2514/5.9781600866319.0450.0458.
- [29] D. D’Humières, I. Ginzburg, M. Krafczyk, P. Lallemand, and L. S. Luo, “Multiple-relaxation-time lattice Boltzmann models in three dimensions,” in *Philosophical Transactions of the Royal Society A: Mathematical, Physical and Engineering Sciences*, Mar. 2002, pp. 437–451. doi: 10.1098/rsta.2001.0955.
- [30] P. Lallemand and L.-S. Luo, “Theory of the lattice Boltzmann method: Dispersion, dissipation, isotropy, Galilean invariance, and stability.”
- [31] Q. Zou and X. He, “On pressure and velocity boundary conditions for the lattice Boltzmann BGK model,” *Physics of Fluids*, vol. 9, no. 6, pp. 1591–1598, Jun. 1997, doi: 10.1063/1.869307.
- [32] M. Geier, A. Greiner, and J. G. Korvink, “A factorized central moment lattice Boltzmann method,” in *European Physical Journal: Special Topics*, 2009, pp. 55–61. doi: 10.1140/epjst/e2009-01011-1.
- [33] K. N. Premnath and S. Banerjee, “On the Three-Dimensional Central Moment Lattice Boltzmann Method,” *J Stat Phys*, vol. 143, no. 4, pp. 747–794, May 2011, doi: 10.1007/s10955-011-0208-9.

- [34] S. V Utyuzhnikov, “Generalized wall functions and their application for simulation of turbulent flows,” *Int J Numer Methods Fluids*, vol. 47, no. 10–11, pp. 1323–1328, Apr. 2005, doi: <https://doi.org/10.1002/flid.873>.
- [35] D. M. Holman, R. M. Brionnaud, and Z. Abiza, “SOLUTION TO INDUSTRY BENCHMARK PROBLEMS WITH THE LATTICE-BOLTZMANN CODE XFLOW.”